Atom/defect classification in Scanning Transmission Electron Microscopy (STEM) Images using Convolutional Neural Networks

Rohan Mewada

A thesis

submitted in partial fulfillment of the

requirements for the degree of

Master of Science

University of Washington

2024

Reading Committee:

Juan-Carlos Idrobo

Ting Cao

Program Authorized to Offer Degree:

Materials Science and Engineering

University of Washington

Abstract

Atom/defect classification in Scanning Transmission Electron Microscopy (STEM) Images using Convolutional Neural Networks

Rohan Mewada

Chair of the Supervisory Committee:
Juan-Carlos Idrobo
Materials Science and Engineering

Two-dimensional (2D) materials have shown great capabilities in various research fields such as physics, chemistry, and engineering because of their low dimensionality and versatility of behavior as compared to their bulk counter parts. Parameters such as twist angles between layers, defect concentrations, and strain can drastically change the properties of the 2D material. To study the interactions inside the 2D material at an atomic scale, the use of electron microscopy techniques such as scanning transmission electron microscopy (STEM) is prevalent in their characterization. However, a bottleneck is hit when it comes to interpreting the STEM image data because of the extent of manual labor and subjective decisions required to segment the atomic columns. Here, a novel approach is proposed for atom/defect classification in STEM images of twisted 2D bilayer materials using deep learning-based image segmentation model. Since it is not feasible to generate a training dataset experimentally, a Python library was developed that leverages the Atomic Simulation Environment (ASE) and abTEM to generate train/test data. This enables the user to easily generate a dataset of their 2D material of interest. For this work, the model was trained on moiré twist angles of 0, 1, and 2 degrees of hBN encapsulated CrI_3 bilayer and demonstrated a remarkable ability to generalize over unknown angles (1.5°, 2.5°, 3.5°, and 4°), thereby showcasing its robustness and versatility. The model precisely segments the atomic columns with a quantification accuracy of 99.27 ± 0.75%. This work highlights the potential of deep learning algorithms in automating and enhancing the analysis of 2D materials, paving the way for more efficient research and product development in the field.

TABLE OF CONTENTS

LIST OF FIGURES

LIST OF TABLES

ACKNOWLEDGEMENTS

I am profoundly grateful for the remarkable individuals I had the privilege to work with at UW. Professor Idrobo has been an extraordinary mentor and guide in my scholarly pursuits and beyond. I will forever be thankful to him for always pushing me to do more without any hint of distress, allowing me to understand my capabilities and interests as I found my path in a foreign land. His wisdom and guidance have been invaluable and supportive. The transformative role of Professor Cao's course, "Data Science and Materials Informatics," in reshaping my perspective on programming, particularly its applications in materials science, cannot be overstated. The course instilled in me the confidence to pick up a project that is focused predominantly on computational science. I would like to thank him for offering his valuable insights and agreeing to be a part of the council. My heartfelt thanks go out to every member of the Idrobo group: Matt Clark, Patrick Kunz, Daniel Salguero, and especially Essance Ray for helping me out immensely with everything related to content. To everyone in the Idrobo group, may your roads lead to warm sands [81].

This thesis would not have come to fruition without the assistance from my non-materials science friends, Pritam Das and Nidhin Harilal. I am grateful to them for hosting "office hours" for all my queries and concerns. A special note of thanks to Nidhin Harilal for his expertise in all things related to neural networks.

For my parents and Anjali: thank you for everything, I cannot begin to say enough about the support you have shown me throughout my Masters. This thesis is not just a testament to my efforts, but a reflection of your faith and belief in me.

DEDICATION

To my parents

and my sister

Chapter 1. TWO-DIMENSIONAL MATERIALS AND IMAGING AT AN ATOMIC SCALE

Since the discovery of graphene, other two-dimensional (2D) materials, such as hexagonal boron nitride (hBN) [1, 2, 3], transition metal dichalcogenides (TMDs) [4, 5, 6], and chromium triiodide (CrI_3) [7, 8], have been the subject of intense research due to their unique properties that differ significantly from their bulk counterparts. The introduction of even minor defects and structural modifications can dramatically alter the functionalities of these 2D materials via strain or doping [9, 10, 11, 12]. The versatility of 2D materials has led to their potential use in a wide range of fields such as flexible electronics [13, 14], biosensors [15, 16], water purification [17, 18], and more. They are also being explored for their potential in quantum photonics [19, 20], optoelectronics [21], quantum computing [22], transistors [23, 24], nonvolatile memory [25, 26], and quantum communication [27, 28].

An emerging field of research is the study of moiré lattices in twisted bilayer 2D material systems [30, 31, 32]. Moiré patterns are interference patterns formed by overlaying similar but slightly offset periodic structures. The relative orientation between two or more layers of a 2D crystal can create these patterns, which have a characteristic size, known as the moiré length, that can be directly controlled by the twist angle between layers. As the moiré length grows, new atomic and electronic phases can emerge to form non-trivial topological states [33, 34].

Structurally, 2D materials are layered crystals that are held together by weak van der Waals forces which can be broken by mechanical exfoliation as shown in the side view of hBN and CrI_3 in figure #. CrI_3 is a 2D material that shows potential in showing the stacking-dependent magnetic order [35, 36] which has a honeycomb network with edge-sharing octahedral coordination as shown in figure 1.1.

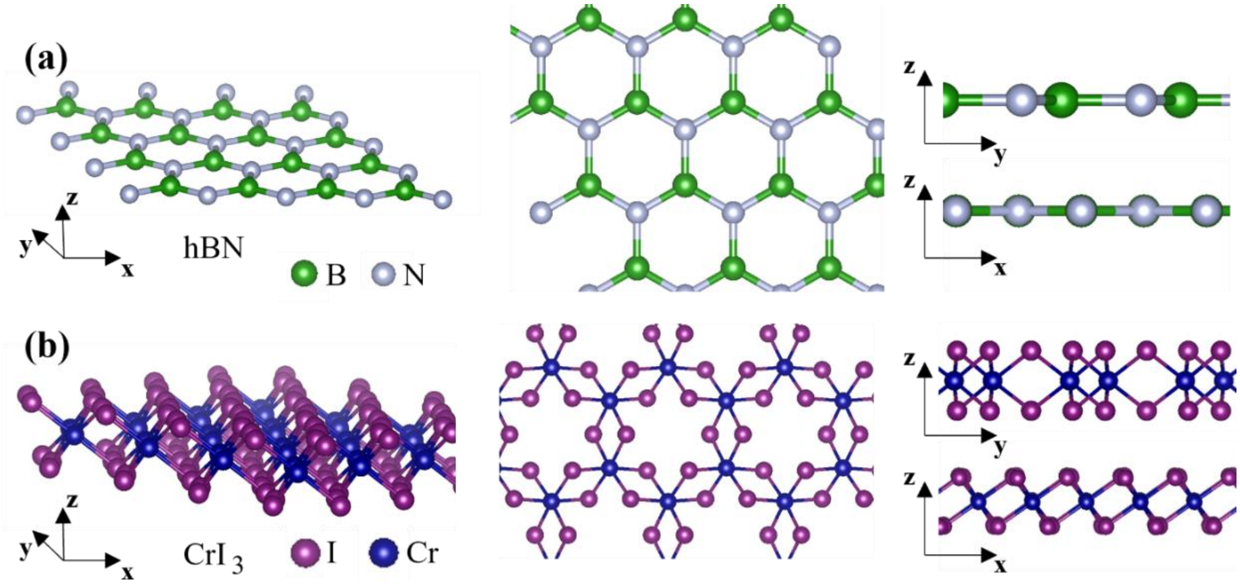

Figure 1.1. Depiction of the crystal structure (isometric, top, and side view) of a) hexagonal boron nitride (hBN) and b) chromium triiodide

Studies have shown that the magnetic properties of CrI_3 are highly sensitive to variations in parameters such as defect concentration [37, 38] and moiré twist angles [39, 40]. Precise control over these attributes is therefore crucial for manipulating the magnetic behavior of this material. For example, when CrI_3 layer stacks are doped with ytterbium (Yb) defects, a robust magnetic interaction is observed between Yb3+ and CrI_3 [41]. This interaction is further influenced by the moiré patterns that emerge in the CrI_3 bilayers [40]. The magnetization of Yb3+ is pinned to CrI_3 by strong superexchange interactions, which contribute an effective internal field of approximately 10 T [41]. This field is greater than the field required for magnetic saturation of paramagnetic Yb3+ and significantly greater than the field required for full CrI_3 magnetization at low temperature (approximately 0.2 T) [41].

In a comprehensive study on intrinsic point defects in single-layer CrI_3 done via Scanning Tunneling Microscopy and Density Functional Theory, exhibit distinct energy levels and spatial distributions for different defect configurations [42]. The most common intrinsic defects identified were single-atom iodine (I) and chromium (Cr) vacancies, along with multiatom CrI_3 vacancies [42]. In the study, it was observed that the energy required to form a CrI_3 vacancy, quantified as 3.36 eV (Figure 1.2d), was only slightly greater than that needed to form a single Cr vacancy (3.29 eV, Figure 1.2b). Notably, the formation energy for $VCrI_3$ was found to be much lower than the combined energy of an individual Cr and three I vacancies (6.52 eV, Figure 1.2c). This indicated that it was energetically more favorable to form a vacancy complex V_{CrI3} rather than creating separate single-atom vacancies [42]. These observations highlight the intricate energy dynamics involved in the formation of vacancies in CrI_3.

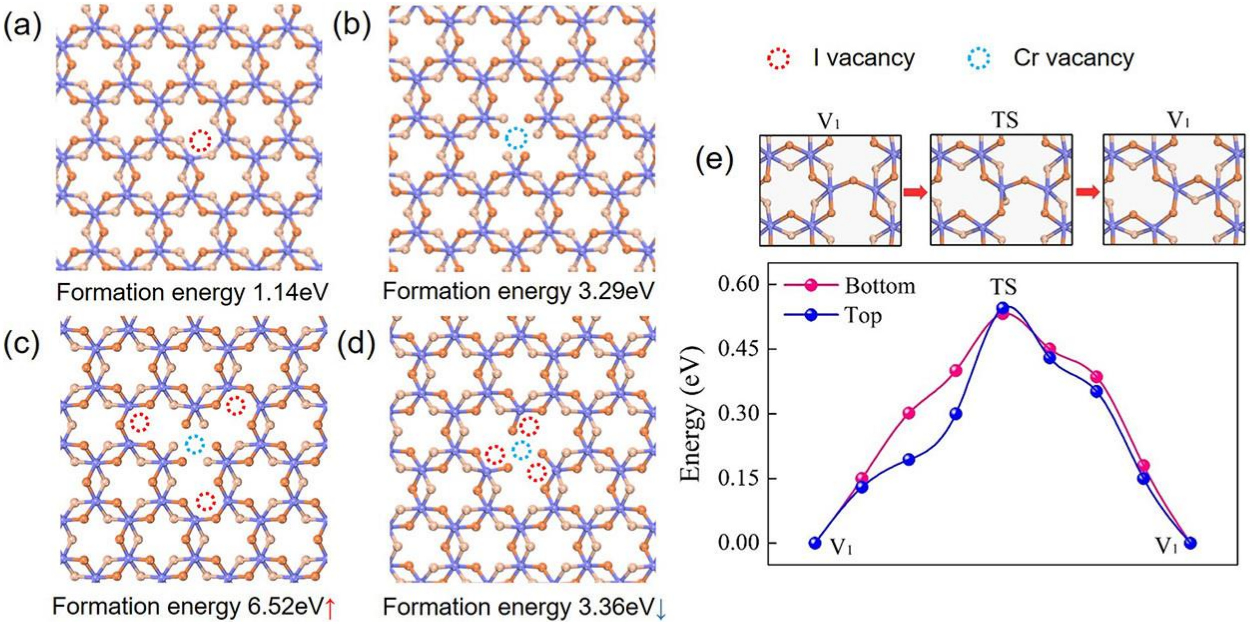

Figure 1.2. Formation energies and I vacancy migration. (a and b) The formation energies for I and Cr vacancy. (c and d) (e) The migration barrier for the I vacancy from both layers. The low-energy barrier indicates the I vacancies are easy to migrate [42]

Their results provide valuable insights into the creation and control of vacancy complexes in single-layer CrI_3. It is known that certain defects in CrI_3 can trigger exotic magnetic states and even flat-band features [43]. In a study by Xu et al., [43] the researchers successfully achieved moiré superlattices in twisted CrI_3 bilayers and unveiled a novel magnetic ground state with coexisting ferromagnetic (FM) and antiferromagnetic (AF) orders. This state could be further modulated by either the twist-angle or electrical gating. The findings shown in figure 1.3 corroborate the formation of AF and FM domains on the moiré length scale, resulting from competing interlayer exchange interactions.

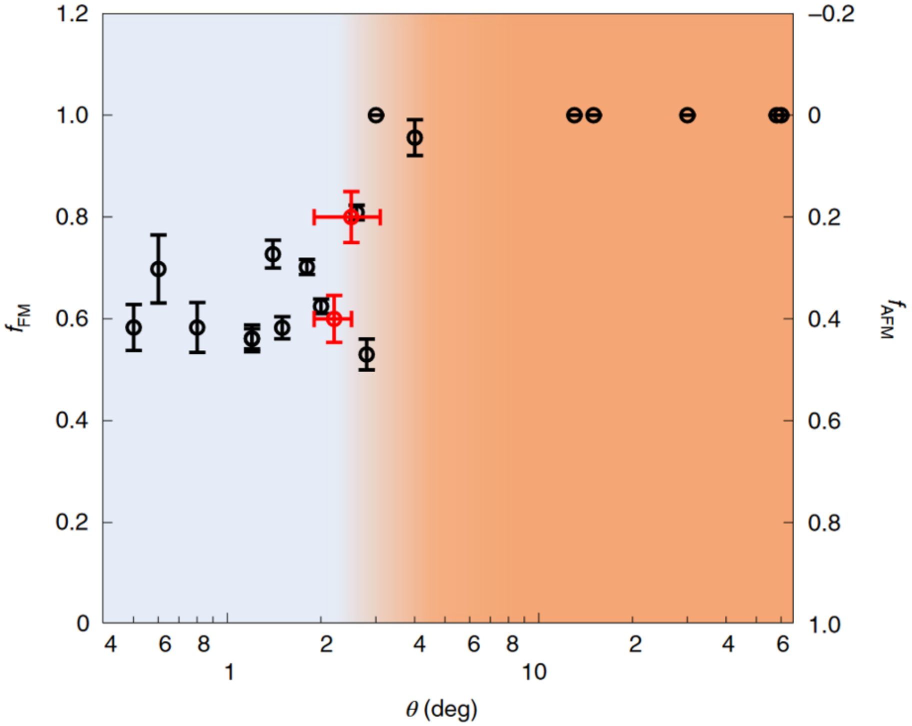

Figure 1.3. The FM and AF fractions, fFM (left axis) and fAF (right axis), as a function of target twist angle θ for all measured samples [43]

The study concludes with a call for high-resolution and high-sensitivity magnetic imaging in future research, to directly illustrate the moiré magnetic textures. These advancements in understanding and manipulating the magnetic properties of CrI_3 pave the way for further exploration and potential applications in the field of 2D magnetic materials.

hBN encapsulated CrI_3 bilayers with a twist angle of 0° (perfectly stacked) are shown in Fig 1.4a. moiré patterns observed in CrI_3 bilayers, are depicted in Figure 1.4b. A 1° twist of the top layer relative to the bottom layer results in a twistronic structure [44]. These structures, featuring randomly induced Yb interstitial and substitutional point defects, served as the basis for our imaging studies.

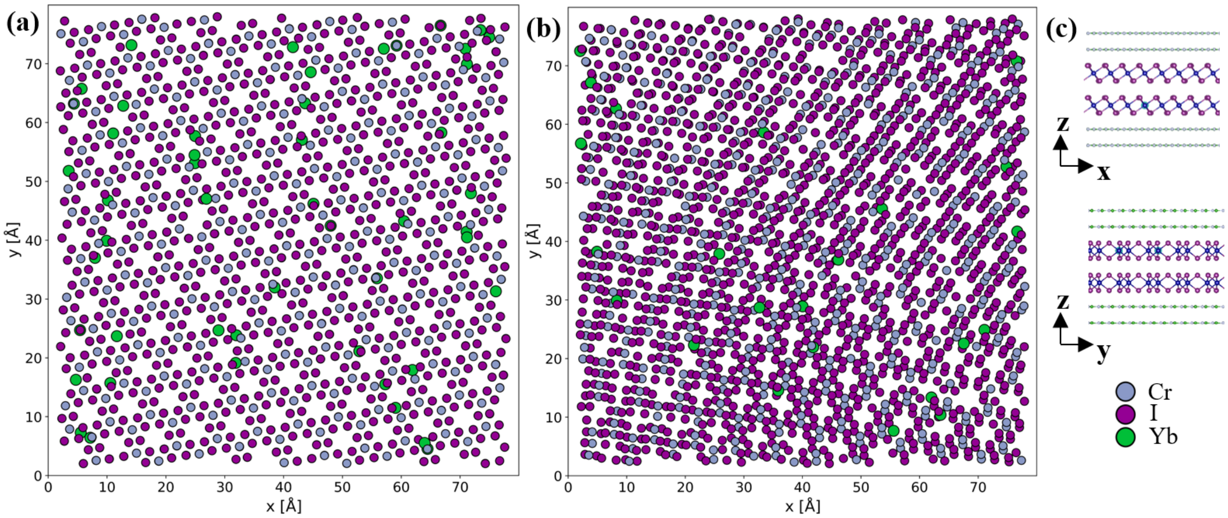

Figure 1.4. Structures for CrI_3 bilayers for (a) 0° and (b) 1° twist angle. (c) cross sections for hBN encapsulated CrI_3 bilayer with 0° twist

1.1 SCANNING TRANSMISSION ELECTRON MICROSCOPY

The understanding of what type of defect is present and resulting in this behavior is still not well understood. As a result, acquiring site-specific information from the specimen is crucial for their characterization. In this regard, scanning transmission electron microscopy (STEM) is a valuable tool owing to the atomic-scale resolution and angstrom-level precision [46, 47].

As depicted in figure 1.5, the cross-section of VG 501 electron microscope (Cavendish Laboratory at Cambridge University) reveals the intricacies of an electron microscope. It employs an electron source under high acceleration voltages to generate an electron beam. This electron beam propagates through a series of magnetic lenses, apertures, and aberration correctors to the sample. The development of the aberration corrector has been instrumental in eliminating the intrinsic aberrations present in the electron beam, a crucial update for achieving a sub-angstrom electron probe size at a relatively lower acceleration voltage [45].

Once the beam reaches the sample, the electrons transmit through interacting with the electrostatic potential of the sample. In the context of transmission electron microscopy (TEM), an electron plane wave is propagated through the region of interest. The electrostatic potential of the atoms causes the incident plane wave to scatter and undergo phase shifts and energy losses during propagation. In contrast, scanning TEM (STEM) uses a focused probe of an electron beam instead of a plane wave. This probe is rastered across the sample, and the deflection of the probe is calculated as a function of the probe position, enabling the acquisition of images at a higher magnification.

The deflected electrons are then collected in one of three types of imaging annular detectors: bright field (BF), annular dark-field (ADF), and high-angle annular dark-field (HAADF). The dark field detectors collect high angle scattered electrons while the bright field collects low angle scattered electrons. Within a STEM, typically an ADF or HAADF imaging is done simultaneously with electron energy loss spectroscopy (EELS) [48] where the high angle scattered electrons are used for the imaging while the low angle electrons are directed into a spectrometer. EELS is a useful technique to utilize for understanding the elemental composition and chemical bonding of the sample [49, 50, 51].

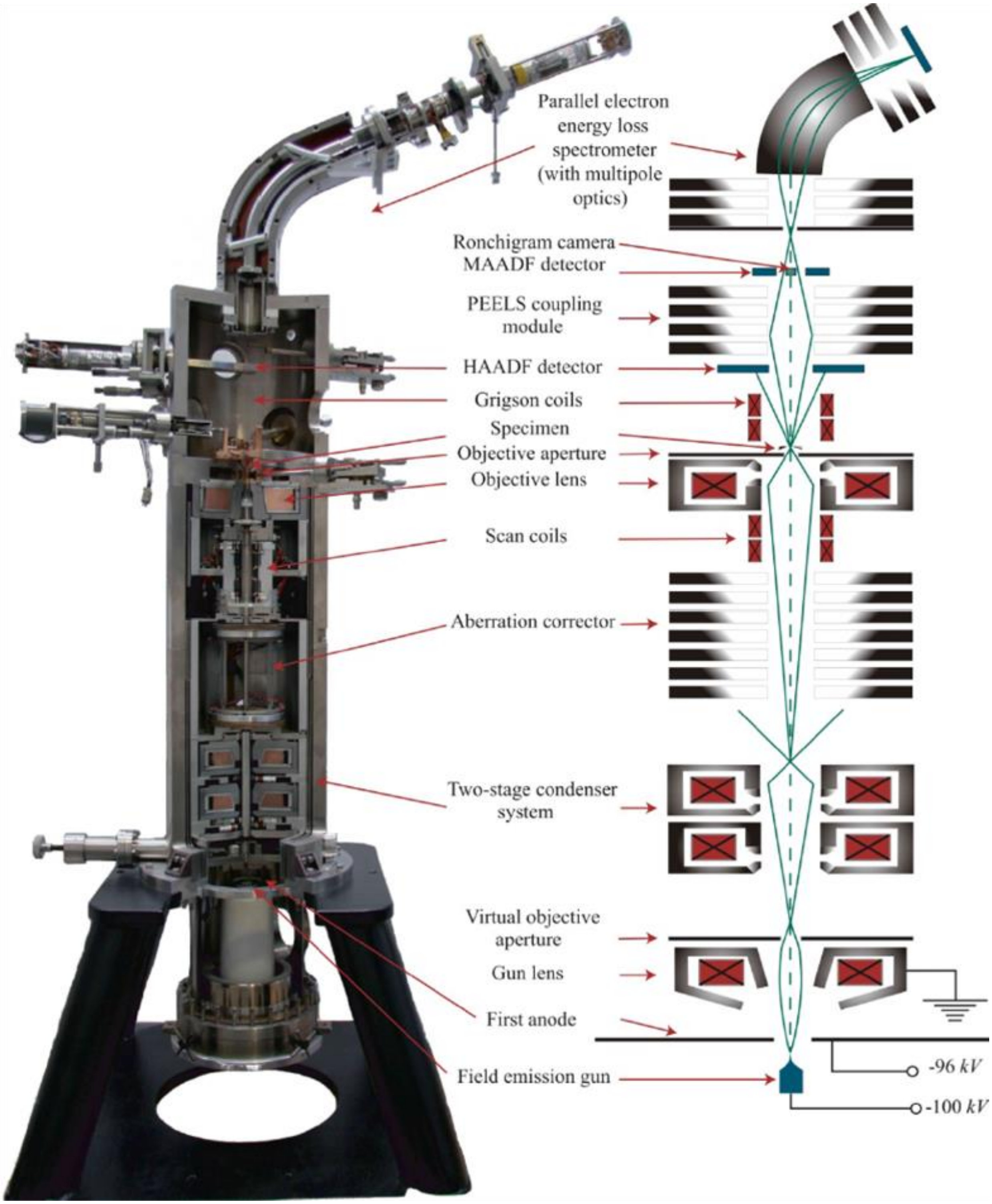

Figure 1.5. Schematic of a VG 501 electron microscope with a detailed component breakdown (Cavendish Laboratory at Cambridge University)

Krivanek et al. observed that the contrast of an atom is directly proportional to the atomic number (I α $Z^{1.64}$) for ADF detectors [52], as illustrated in figure 1.6. This relationship enables researchers to quantify atomic columns and structural parameters using image analysis techniques that focus on comparing contrasts in experimental images with simulations. However, such techniques have inherent limitations and require substantial manual labor. Furthermore, since the analysis is subjective, it can often lead to ambiguous interpretations, particularly in cases where the contrast is non-uniform or different atomic columns exhibit similar contrast.

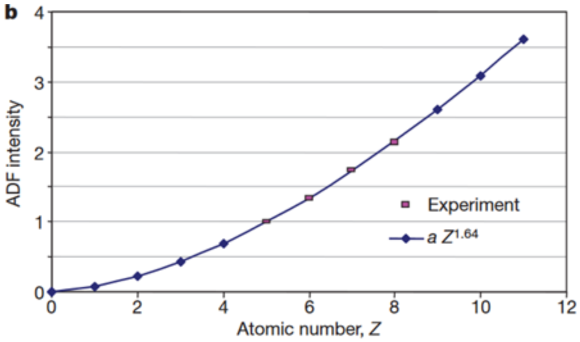

Figure 1.6. Plot of the relationship between the intensity of electrons detected by an annular dark-field detector (ADF) and the atomic number of an element [52].

1.2 MULTISLICE SIMULATIONS

To illustrate how the limitations of atomic detectability are a problem, STEM images of Yb-doped hBN-CrI_3 bilayers were analyzed. In order to create the STEM images, multislice simulations [53] were used. In the quantum regime, electrons can be conceptualized as waves, which enables the simulation of TEM/STEM images by approximating the incident electron wave as a wave function. This wave function can be propagated through a potential map, which is generated using the electrostatic potentials of a structure. These simulations are referred to as multislice simulations.

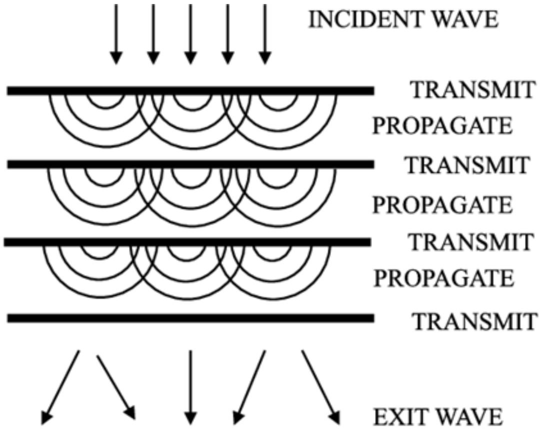

Figure 1.7. Depiction of a multislice simulation where the plane wave transmits and propagates through the sample [54].

To perform multislice simulations, the sample is segmented into slices divided along the direction of electron beam propagation. A potential map is then generated for each slice using the electrostatic potential of the atoms present. Figure 1.7 illustrates a schematic for TEM multislice simulation, where an incident plane wave is propagated through a series of slices. This results in an exit wave after each slice, which is used as the incident wave for the subsequent slice. The exit wave function ($\psi_{n+1}(\vec{r})$) after the nth slice can be determined by using equation 1 [56].

$$\psi_{n+1}(\vec{r}) = p(\vec{r}) * [\, t_n(\vec{r})\, \psi_n(\vec{r})] \tag{1}$$

$$p(\vec{r}) = \frac{1}{i\lambda\Delta z} \exp\left[\frac{i\pi}{\lambda\Delta z} r^2\right]$$

$$t_n(\vec{r}) = \exp\,[i\sigma V_n(\vec{r})]$$

In this context, $p(\vec{r})$ represents the Fresnel free-space operator, and $t_n(\vec{r})$ applies a phase shift to the incident wave ($\psi_n(\vec{r})$) that is proportional to the potential of the slice ($V_n(\vec{r})$). The convolutions are computed as a multiplication in Fourier space through a sequence of forward and inverse Fourier transforms. For performing such multislice simulations, there are several open-source tools available, such as QSTEM [55] and abTEM [56]. In this study, abTEM, has been utilized and the specifics of which will be elaborated on in further sections.

The choice of abTEM is motivated by its flexibility in implementing a range of STEM features such as the contrast transfer function (CTF), and its adaptability in defining parameters, among other features. A significant advantage of abTEM is its capability to be parallelized over GPU with minimal effort, a feature facilitated using Dask [57].

Multislice simulations are notably computationally demanding as each probe position, which can easily number in the millions, necessitates its own multislice probe propagation. Therefore, GPU parallelization can markedly reduce the simulation time by performing calculations on a batch of probe positions concurrently. While the simulation cannot be parallelized in the direction of wave propagation (as the exit wave after each slice is dependent on the exit wave function of the previous slice), it can be parallelized over probe positions within a single slice.

Using abTEM, STEM images of Yb-doped hBN-CrI_3 bilayers were generated for a 0° twist angle between CrI_3 monolayers. Four different Yb defect configurations were analyzed: (a) two interstitial Yb defects (Yb_I) in AA stacking (b) two interstitial Yb defects (Yb_I) in AB stacking (c) two substitutional Yb defects (Yb_{Cr}) in AA stacking and (d) two substitutional Yb defects (Yb_{Cr}) in AB stacking.

1.3 DETECTABILITY OF ATOMIC COLUMNS IN A STEM IMAGE

Figure 1.8 provides a depiction of the intensity profiles across the said four defect configurations. From Figure 1.8a, it is evident that there exists a clear correlation between the atomic number and the maximum intensity of the atom. In this figure, two Yb interstitial point defects are perfectly stacked, resulting in a higher intensity observed at the center compared to that at the center of two perfectly stacked I atoms.

This observation is further corroborated by Figures 1.8b and c, where the identification of Yb can be straightforwardly achieved by considering the intensity alone. However, in Figure 1.8d (area highlighted in red), the Yb atom in the top layer exhibits an intensity that matches the intensity of the I columns surrounding it. In such scenarios, relying solely on comparing intensities proves insufficient. Instead, we would need to compare the full-width half-maximas (FWHM) of the Gaussians formed by the atomic column's intensity profile. By comparing the FWHM of different atomic columns, we can differentiate between atoms that have similar intensities but different atomic structures since columns with bigger atoms would have a larger value of FWHM.

Some of the ways a researcher can expedite the analysis process is by relying on mathematical models focused around obtaining local peak maxima and the respective contrast or applying fast fourier transform [58, 59]. Although such methods can be used to make the classification task easier, these methods tend to not generalize over images taken under different microscope settings, and often require manual tuning of the algorithm. Due to the subjective nature of the classification task, even an experienced researcher can be prone to factors such as misinterpretation, human bias and error.

On this front, machine learning (ML) algorithms have been pivotal in transforming various other fields that demand object detection, segmentation, and recognition [60, 61, 62, 63]. A further subset of neural networks is deep learning algorithms. Bolstered by the increased availability of high-power GPUs, deep learning has made a profound impact in the field of Computer Vision.

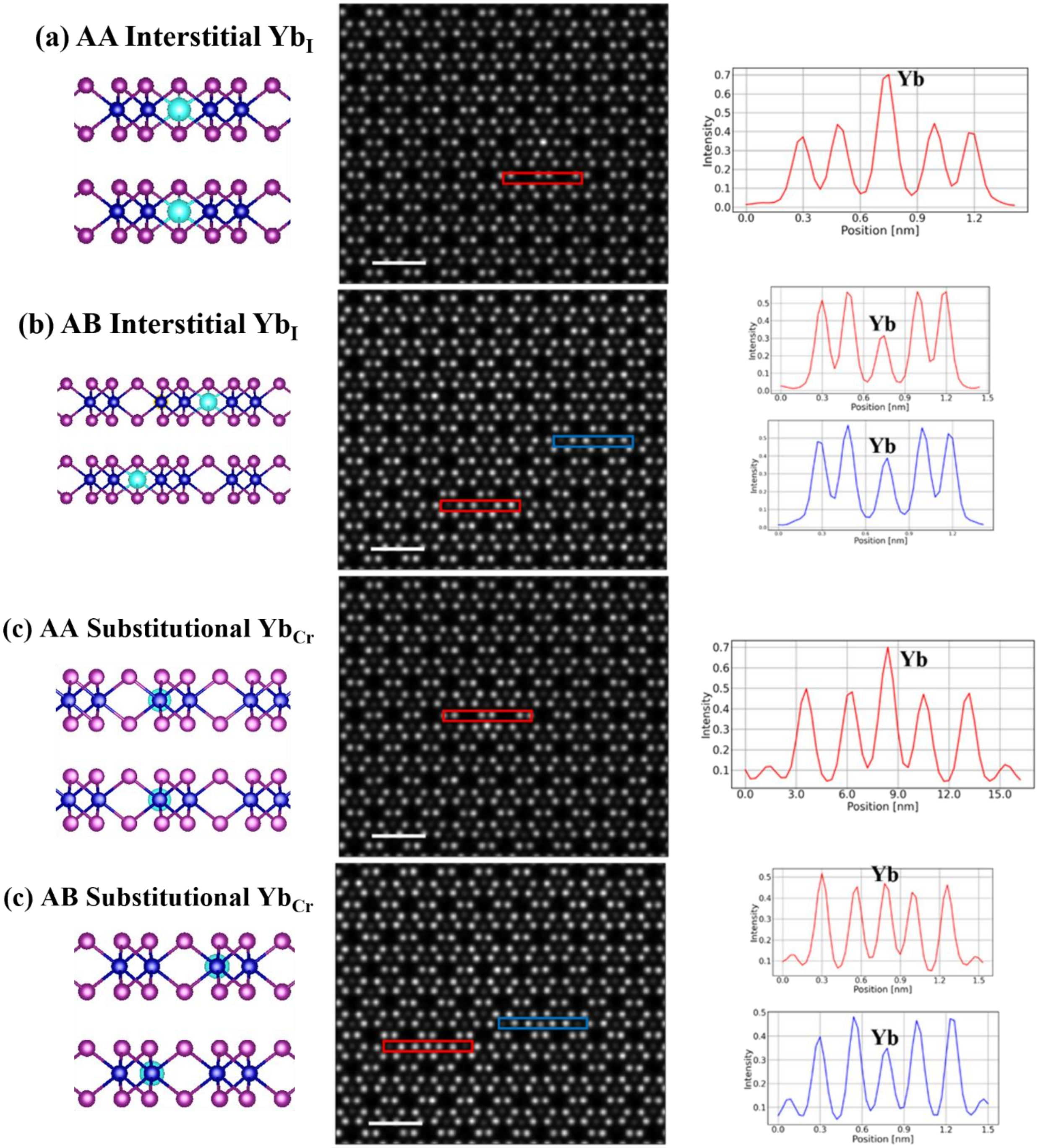

Figure 1.8. Illustration of detectability for (a) ytterbium interstitial (Yb$_I$) in AA-stacking (b) Yb$_I$ in AB-stacking (c) ytterbium substitutional (Yb$_{Cr}$) in AA-stacking (d) Yb$_{Cr}$ in AA-stacking. (left) structure (center) STEM image simulation (right) intensity profile of highlighted region

1.4 CONVOLUTIONAL NEURAL NETWORKS

Central to these developments are Deep Convolutional Neural Networks (CNNs). CNNs are designed for tasks that demands a deep understanding of intricate details and context from images. A prime example of a deep CNN architecture is the U-Net, that has made significant strides in the field of image segmentation. Developed at the Computer Science Department of the University of Freiburg, U-Net was originally designed for biomedical image segmentation [64]. The architecture's design is characterized by its unique U-shaped structure, which allows for precise localization combined with contextual information from images, making it highly effective for segmenting intricate structures in biomedical imagery. However, its effectiveness has led to its application in a variety of other domains as well [65, 66, 67].

Convolutional Neural Networks (CNNs) like the U-Net essentially automate and enhance the process of feature extraction from images, a task that is often performed manually in various scientific fields, including STEM. As discussed previously, researchers sometimes rely on statistical models for expediting STEM image interpretation [58, 59]. However, these techniques are often limited in their ability to effectively extract and distinguish features with complex inherent atomic contrast.

On the other hand, CNNs automate the feature extraction process by learning to extract a hierarchy of features from the raw pixel data. This automated process is exemplified in the convolution operation, a fundamental building block of CNNs. Figure 1.9 shows a convolution operation for enhancing circular features in a simulated STEM image of hBN-CrI_3 bilayer. Moreover, CNNs can learn to extract a much wider variety of features compared to manual techniques, and they can do so more consistently and extensively [68, 69]. This makes them particularly effective for tasks such as semantic segmentation where the objective is to assign a class to each pixel in the image, necessitating the extraction and interpretation of a wide array of features at different scales and complexities.

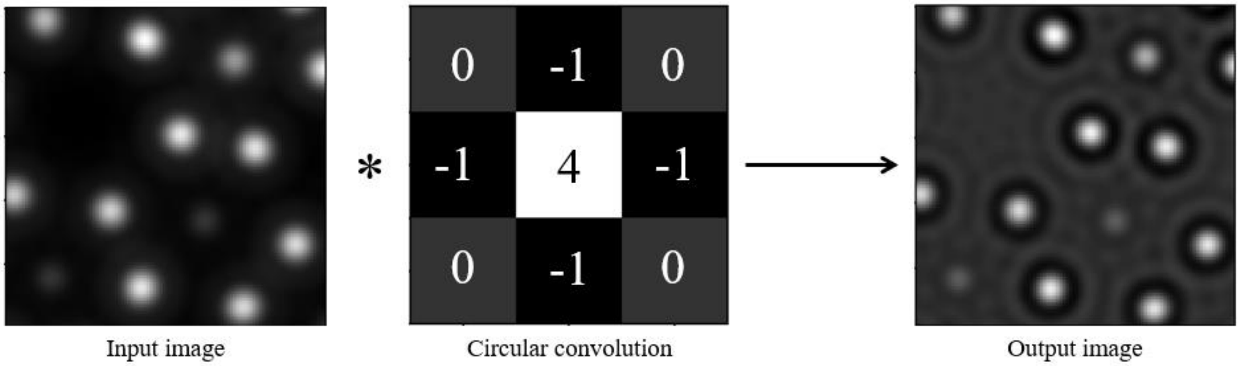

Figure 1.9. Illustration of 3x3 convolution operation for enhancing circular artifacts in a 100x100 input image taken from a region in figure 1.8.

Some of previous work on classification of atomic columns using neural networks [70, 71, 71] have followed a similar approach of using simulations as a part of their training data [70, 71]. For instance, a study conducted by Yang et al. [70] demonstrated the use of Annular Dark Field (ADF) image simulations calculated using Quantitative STEM (QSTEM) software for generating their training data. This approach underscores the potential of integrating simulation data with machine learning techniques for efficient and accurate analysis of atomic structures in 2D materials. The performance of the algorithm was demonstrated by efficiently quantifying a variety of defects and dopants in quintessential 2D TMD monolayers and their doped forms (WSe_2, MoS_2, V-doped WSe_2, and V-doped MoS_2). The accuracies achieved were comparable to that of human-based data interpretation for monolayers. Their implementation of the automated quantification algorithm demonstrated that it could efficiently process a substantial amount of raw data (comprising 60 stacked ADF images) in less than 3 minutes. In contrast, a human working at a constant speed might require approximately 60 hours to accomplish the same task. This highlights the significant efficiency and time-saving potential of their automated algorithm.

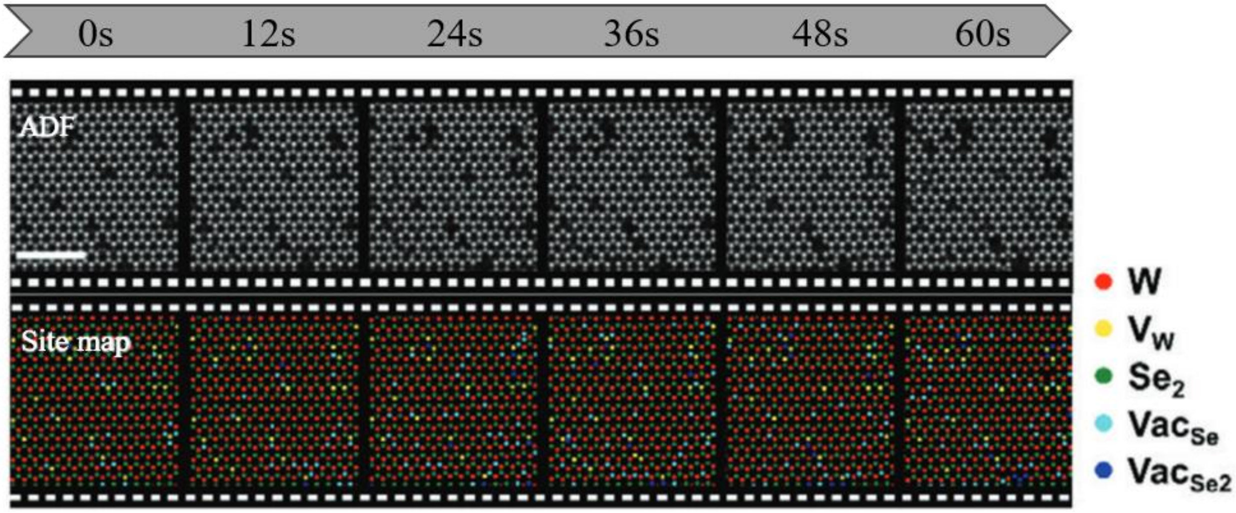

Figure 1.10. Application of the automated quantification algorithm to large imaging data volumes of (doped) WSe2showing dynamic defect evolutions under electron beam irradiation. (top) Series of ADF STEM images of pristine WSe2 and V-WSe2 sequentially recorded under electron beam irradiation and (bottom) corresponding atom-site classification maps obtained from the established deep learning algorithm [70]

Another recent study by [71] reported the development of a training library and a deep learning method capable of performing robust and precise atom segmentation, localization, denoising, and super-resolution processing of experimental images.

Interestingly, despite the use of simulated images as training datasets in these studies, the deep learning model demonstrated the ability to self-adapt to experimental STEM images. It exhibited exceptional performance in atom detection and localization under challenging contrast conditions, consistently outperforming the precision of the state-of-the-art two-dimensional Gaussian fit method.

Both of the above referenced studies have incorporated their unique denoising models to enhance the signal-to-noise (SNR) ratio, a critical factor influencing the performance of any classification model. A more detailed discussion on this topic is presented in chapter 4.

Furthermore, these studies have employed a U-Net architecture Convolutional Neural Network (CNN) for their models, owing to the previously discussed benefits.

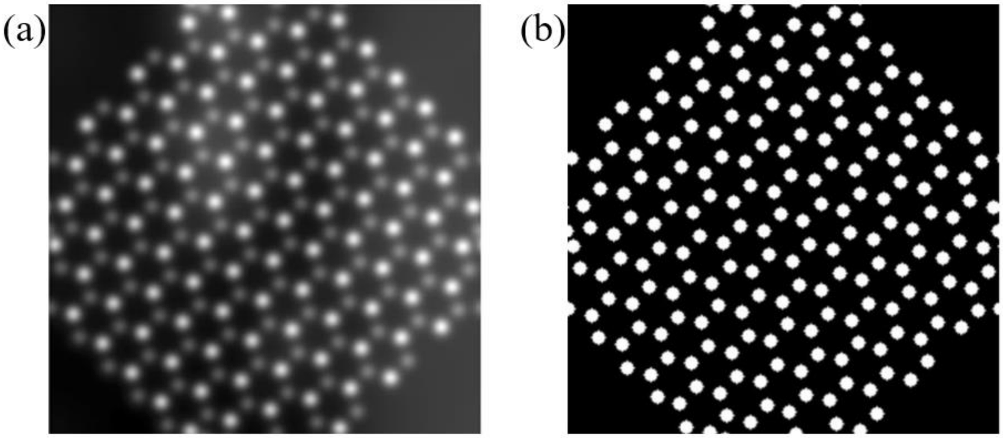

Figure 1.11. (a) denoised STEM image with (b) atomic-column segmentation [71]

Chapter 2. ATOM-INATOR

Using the results and observations from chapter 1, we developed our own automated workflow for training a STEM image segmentation model for twisted bilayers of hBN encapsulated CrI_3 with Yb defects. We have relied on abTEM for generating the train and test dataset for training our deep CNN with a U-Net architecture.

2.1 U-NET

The U-Net architecture, a type of encoder-decoder network, is characterized by its symmetric structure. The encoder, also known as the contracting path, is responsible for contextualizing the input image. This is achieved by reducing the spatial resolution while simultaneously increasing the depth through a series of convolutional and max pooling layers. This process effectively distills the information into a more compact, lower-dimensional form known as the latent space, which encapsulates the image's most crucial features.

Data contextualized in this compact state is then passed onto the decoder, or the expansive path. The decoder's role is to reconstruct another image back from this compressed form that we call latent space, focusing on locating key features while simultaneously increasing (referred to as upsampling in the ML literature) the image's spatial resolution. It does this upsampling of the latent space feature maps by applying convolutional operations in the expansive path.

A key component of this architecture is the integration of skip connections from the contracting path to the expansive path. They help to preserve the spatial information that might be lost in the contracting path. By channeling this information to the decoder layers, they enhance the network's ability to accurately locate and manipulate the important features in an image. This interplay between information compression and decompression allows the U-Net architecture to effectively process and analyze complex image data.

U-Net effectively leverages the benefits of a fully convolutional network, while also addressing the challenge of precise localization, which is often a problem in semantic segmentation tasks. This effectiveness in handling precise localization motivates us to employ U-Net for STEM images. Figure 2.1a depicts the schematic of the U-Net used in this study. We decided to use a relatively deeper architecture, with three downsampling layers, which consequently necessitates three corresponding skip connections and upsampling layers. This design choice was determined by taking into account the number of classes we wanted to classify. For the specific case of hBN-CrI_3 bilayer with Yb doping, nine different atomic columns are present as shown in figure 2.1b and c. Hence, including the background as one class and adding an additional class for "unidentified" elements, the total classes in our case is eleven.

Figures 2.1b, c shows the goal of the work in this thesis. We desire to develop a U-Net based CNN which can give us a pixel-wise classification map of the atomic columns present in the image. Using the classification map, we can obtain quantitative information about the distribution of the columns.

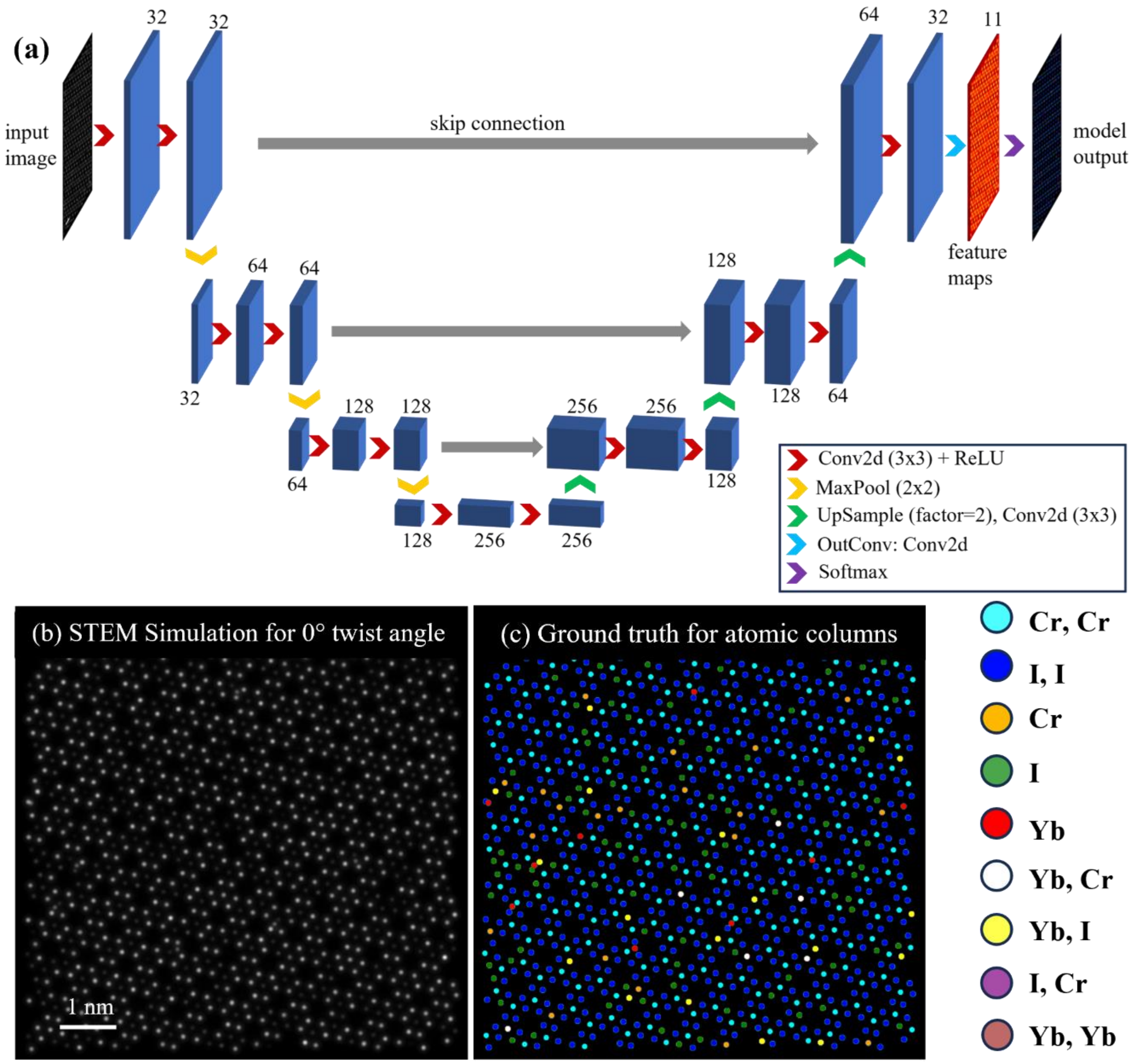

Figure 2.1. (a) Schematic of the U-Net architecture used for classification (b) simulated STEM image of hBN-CrI_3 with 0° twist angle (c) ground truth for atomic columns present in the image

However, researchers working on developing STEM image classification models hit another bottleneck, that is the generation of diverse training data. Acquiring images for training a CNN can be very expensive in terms of manual labor and time required. To allow the model to generalize over unknown atomic configurations, it is imperative for the dataset to be sufficiently large and inclusive of various crystallographic orientations. In addition to this, generating the labels for the images would introduce its own complications due to reasons discussed previously.

Hence, our model's accuracy would be limited by the error rate involved in manually generating/labelling the dataset. This essentially makes it impossible for us to experimentally generate a reliable training dataset.

To overcome the complications related to the training dataset generation, we have relied on multislice simulations. Specifically, we have used abTEM to automate the dataset simulation workflow. abTEM is a Python-based multislice image simulation package that seamlessly merges Density Functional Theory (DFT) and other atomistic modeling methods with electron scattering simulation [56].

2.2 GENERATING TRAINING DATA

It is important to address the complications related to simulating a training data. Even simulated training data can exhibit bias, particularly related to the workflow of the training process, such as the basis structure used for simulations. To counteract this bias, we have introduced a significant degree of randomness into the generation workflow, while ensuring the maintenance of a realistic crystal structure.

Moreover, it has been noted that the perceived atomic column positions in Annular Dark Field Scanning Transmission Electron Microscopy (ADF-STEM) images may not always align with the actual positions [73]. This phenomenon, particularly prevalent in a quantum regime, is heavily influenced by the attributes of the specimen's lattice and the imaging environment.

Nevertheless, as discussed further in chapter 3, our model has demonstrated its ability to generalize atomic columns over unknown atomic orientations. This indicates that the model successfully achieves its objective of image classification, irrespective of the atomic structure.

Our proposed methodology has the potential to automate the generation of datasets for a variety of 2D stackings, necessitating only a unit-cell of the materials of interest. For the sake of simplicity and consistency, we have selected Ytterbium (Yb) doped hexagonal boron nitride (hBN) encapsulated chromium triiodide (CrI_3) twisted bilayers as the subject for our model's development and analysis.

The Atomic Simulation Environment (ASE) [74] and NumPy [75] were utilized for the manipulation of unit-cells to assemble, rotate, and stack monolayers of hBN and CrI_3, as shown in figure 2.1. A random assortment of defects such as Yb interstitial, Yb substitutional, and vacancies of Cr and I were introduced through a series of operations. In order to augment the diversity of the dataset, the entire stack was rotated and a field of view measuring 8nm x 8nm was extracted. The final 8nm x 8nm structure was then employed to establish the ground truth of the simulation via abTEM.

Table 2.1 illustrates the degree of randomness incorporated into the dataset generation workflow, with a uniform distribution across all cases. For twist angles, it is observed that accounting for all possible permutations of atomic columns is necessary. In our scenario, by merely incorporating three twist angles (0°, 1°, and 2°) between CrI_3 monolayers, the model demonstrated the ability to generalize over unknown twist angles, a topic further explored in the results section.

Key parameters that influence both the quality of the final image and the simulation time include slice thickness, sampling, and the number of frozen phonon configurations. These parameters were selected following a series of benchmarking tests aimed at optimizing simulation time without compromising the quality of the resulting image. In terms of sampling, the Nyquist frequency [76] of the probe was chosen, as mentioned in table 2.2.

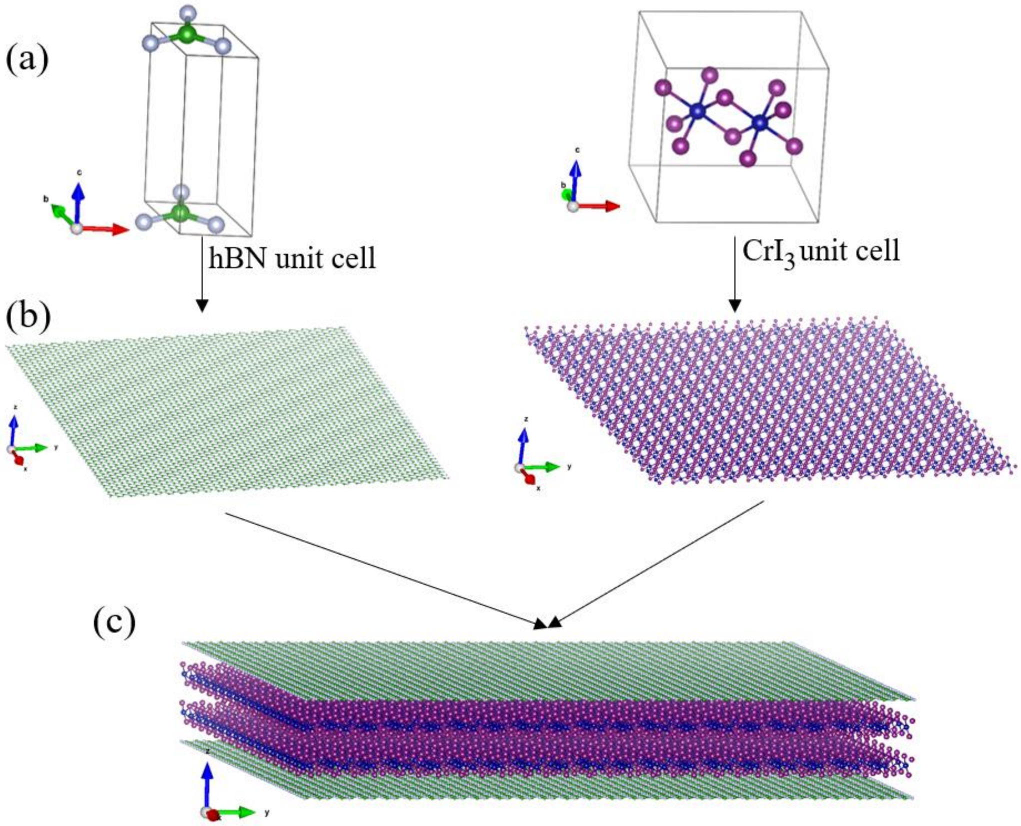

Figure 2.2. Schematic of the automated structure generation workflow: (a) Unit cells for hBN and CrI_3 (b) monolayers generated using the unit cells (c) hBN encapsulated CrI_3 bilayer structure formed by stacking the monolayers

Table 2.1. Degree of randomness incorporated in structure generation of hBN-CrI_3 twisted bilayers

Parameter/operation	**Distribution**
Twist between CrI_3 monolayers	0°, 1°, 2°
Yb substitutional defects	0 to 50
Yb interstitial defects	0 to 50
Cr vacancies	Up to 10%
I vacancies	Up to 10%
Full stack rotation	0° to 360°

Table 2.2. simulation parameters used for STEM mode in abTEM

Simulation Parameter	Value
Acceleration voltage	100 keV
Semi-angle cutoff	30 mrad
Detector angle	80 to 120 mrad
Sampling	0.3 Å
Slice thickness	2 Å
Frozen phonon instances	3
Field of view	80 Å x 80 Å

In the final stages, the outputs from the simulation are interpolated to achieve a sampling of 0.076 Å, resulting in a 1024x1024 pixel image for an 8nm x 8nm field of view. The output from abTEM, which is in the .zarr format, is then converted into a numpy array. This process is repeated for a pre-defined number of iterations (size of training data).

2.3 PARALLEL PROCESSING IN ABTEM VIA DASK

A significant portion of the computations in abTEM are embarrassingly parallel. For instance, each probe position is independent, allowing each CPU core to calculate a batch of positions independently, requiring communication only upon the completion of a run of the multislice algorithm. The parallelization of abTEM is achieved using Dask, a flexible Python library for parallel computing [57]. Dask enables scaling from a single laptop to hundreds of nodes at high-performance computing (HPC) facilities with minimal code modifications.

This functionality facilitates the simultaneous execution of multislice calculations over a batch of probe positions. In this study, the maximum batch size for a chunk was set to 1000, dividing the entire calculation array into 507 chunks, as indicated in the table. In the case of a single CPU, abTEM is required to process 4.78TiB of data. This data size is specific to the parameters defined in the table 2.2.

Discussing in terms of the number of wave functions calculated, for a single CPU, if every probe position is calculated on one processor, abTEM would process a wave function ensemble of size (3, 390, 390, 1200, 1200). Here, (1200, 1200) represents the resolution of our image, (390, 390) are the probe positions, and 3 is the number of frozen phonon instances, all within a single slice. Consequently, it would need to process 456,300 probe positions individually.

However, when utilizing a Nvidia A100 GPU with 80GB memory, 1000 probe positions can be calculated simultaneously, resulting in a total of 507 chunks (The access of GPU was facilitated by Hyak, University of Washington's [80] supercomputing clusters). This demonstrates the efficiency and computational power of parallel computing in handling large-scale calculations in abTEM. As a result, the simulation time was improved by a factor of 237, as observed in table 2.3. Because of the higher throughput, the parallelization will be more effective in cutting down simulation times with larger lattices. This demonstrates the efficiency and computational power of parallel computing in handling large-scale calculations in abTEM, which allows us to generate a large training dataset.

Table 2.3. Comparison of simulation array and time for type of processor used

Processor	Chunks calculated in one slice	Simulation time
Single CPU	456,300	12 hours
Nvidia A100 80GB GPU	507	182 seconds

The training dataset created for this study comprised images simulated at three twist angles: 0°, 1°, and 2°. For each twist angle, 200 images were generated for the training set and 100 for the test set. This resulted in a total of 600 labeled images for training and 300 for testing. To augment the dataset and enhance the robustness of the model, simple symmetry operations, such as horizontal and vertical flips, were applied during the training loop. This effectively quadrupled the size of both the training and testing datasets.

Figure 2.2 provides an example for two of the three twist angles (non-zero) included in our training dataset. Upon examination of the figure, it becomes evident that there is a significant class imbalance between the atomic columns containing Yb defects ([Yb, Cr], [Yb, I], [Yb], [Yb, Yb]) and atomic columns related to the bulk ([Cr, Cr], [I, I], [Cr], [I]). This imbalance can introduce complications during the training process, as the model has a significantly larger number of features for the bulk columns to learn from, compared to the relatively few atomic columns associated with the Yb defect. To address this issue, it may be beneficial to increase the defect concentration during training or to explore the use of weighted loss [77].

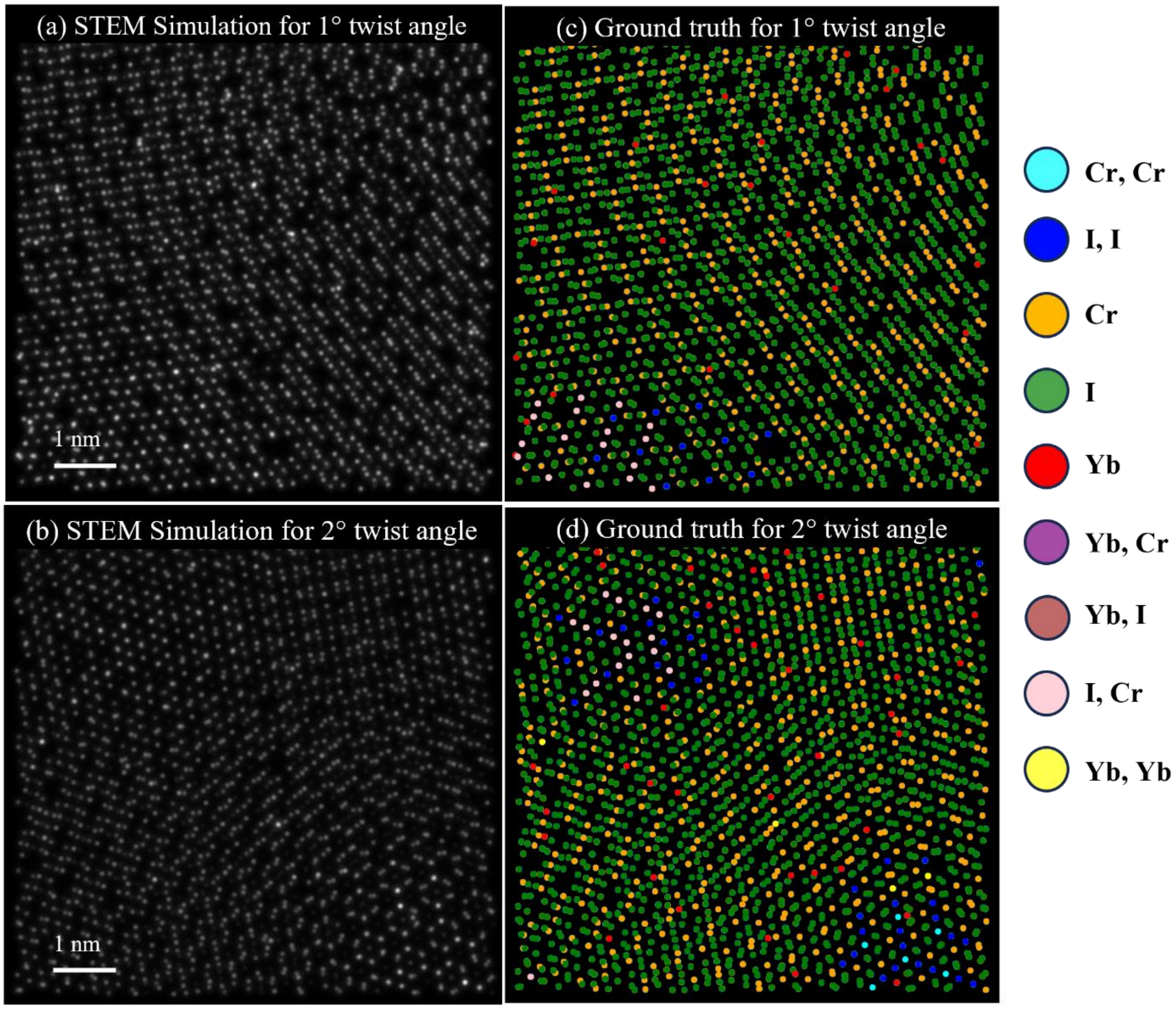

Figure 2.3. Examples of STEM image simulation and the atomic column ground truth for (a, c) 1° twist and (b, d) 2° twist angles

Table 2.4 shows the values of hyperparameters utilized during the training of the model. Among the 11 classes, class 0 is designated for the background, while class 10 corresponds to unidentified atomic columns. It was noted that a learning rate of 0.0005 was adequate to achieve convergence of train/test loss after approximately 25 epochs.

Table 2.4. Hyperparameters defined for training the U-Net

Hyperparameter	**Value**
Batch size	8
Input/output resolution	1024 x 1024 pixels
Number of classes	11
Epochs	300
Learning rate	0.0005

The size of the classification circle on the ground truth is a crucial aspect to consider. In our approach, we have selected the circle size to encompass the largest atom present in the image, which in this case is Ytterbium (Yb). As depicted in the figure 2.3, there may be instances in moiré structures where atoms at varying column heights overlap but are not perfectly stacked. In such scenarios, the atom would still be classified, albeit into a different class. For instance, two individual I atoms (green) would be classified under the [I, I] class (blue) after a threshold of 0.3 Å.

In this thesis, have successfully devised an automated approach for training a U-Net model for the classification of atoms and defects across a range of 2D stackings and heterostructures. Our methodology, when applied to Yb-doped CrI_3 twisted bilayers encapsulated with hBN, has proven its capability to accurately segment atomic columns. Upon evaluating 162 new images and 216,869 atomic columns in total, an average quantification accuracy of 99.27 ± 0.75% was obtained. It's important to highlight that all the STEM images used in this study were simulated using abTEM, and the stated accuracy was derived from predictions on the test data.

Furthermore, we utilize the classification map to determine the count of atomic columns. This enables us to ascertain both the concentration of defects and the distribution of atomic columns, providing valuable insights into the material's structure and composition.

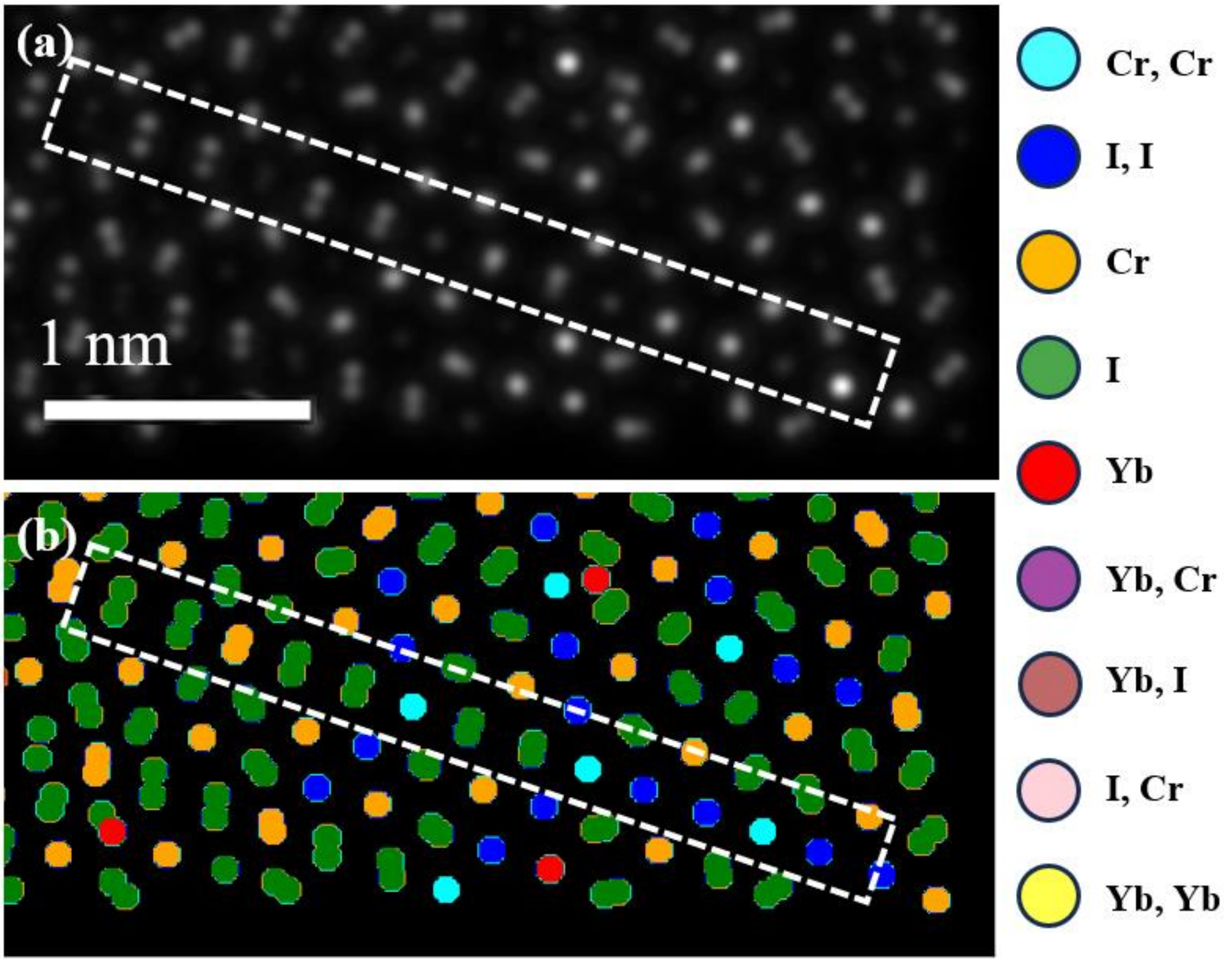

Figure 2.4. Snapshot from (a) simulated STEM image of hBN-CrI_3 with 2° twist and Yb defects and (b) ground truth of the same region. White box depicts the atom classification trend for overlapping atoms

Chapter 3. RESULTS AND DISCUSSIONS

While previous work on similar deep Convolutional Neural Networks (CNNs) for monolayers have incorporated Density Functional Theory (DFT) calculations into their dataset simulation workflow [70], we have chosen to exclude this step. This decision was based on the consideration that DFT calculations are not particularly relevant for training a model developed for pixel-wise classification. Furthermore, our model is already exhibiting signs of generalization. As such, the inclusion of DFT calculations, which might result in minor shifts in atomic positions, would likely be redundant and would not significantly impact the classification of atomic columns.

3.1 U-NET CLASSIFICATION RESULTS

The atomic column prediction map, as shown in figure 3.1a, is a product of our U-Net model. The model accurately maps atomic columns, even in areas where ambiguity is present (such as clusters of a few atoms). This allows the model to provide critical information on local non-stoichiometry with a resolution of 0.3 Å. Such site-specific information is essential for understanding the optical, electronic, and magnetic properties due to the strong coupling within the lattice and defects, especially in moiré lattices [78].

However, on comparing figure 3.1b and d, while an atomic column is detected, it is seldom misclassified when compared to the ground truth. Such instances have been consistently observed in the test data predictions. This could be attributed to the significant class imbalance. Class imbalance is a common and a challenging problem in classification tasks of ML, which can lead to models being biased towards the majority class and performing poorly on minority classes, often resulting in misleading performance and a lack of generalization. For instance, there are 1060 atomic columns belonging to class [Cr, Cr] and [I, I] combined, and in case of atomic columns pertaining to defects ([Yb, Cr], [Yb, I], [Yb]), there are 55 atomic columns. This difference implies that there are not sufficient examples to learn from for the defect classes, compared to the bulk atomic columns.

Figure 3.2 depicts the train/test loss vs epoch curve for the training of our U-Net. As a reminder, the training was conducted with a batch size of 8 and a learning rate of 0.0005. The gradual convergence of the test loss with the train loss could suggest that the model primarily learns to classify the bulk columns during the initial 25 epochs, and the remaining epochs are utilized for segmenting the defect classes. Therefore, it might be beneficial to use a higher defect concentration during the dataset generation pipeline. The rapid convergence also suggests that if the issue of class imbalance is addressed, comparable or even superior classification results could be achieved using a smaller train/test dataset.

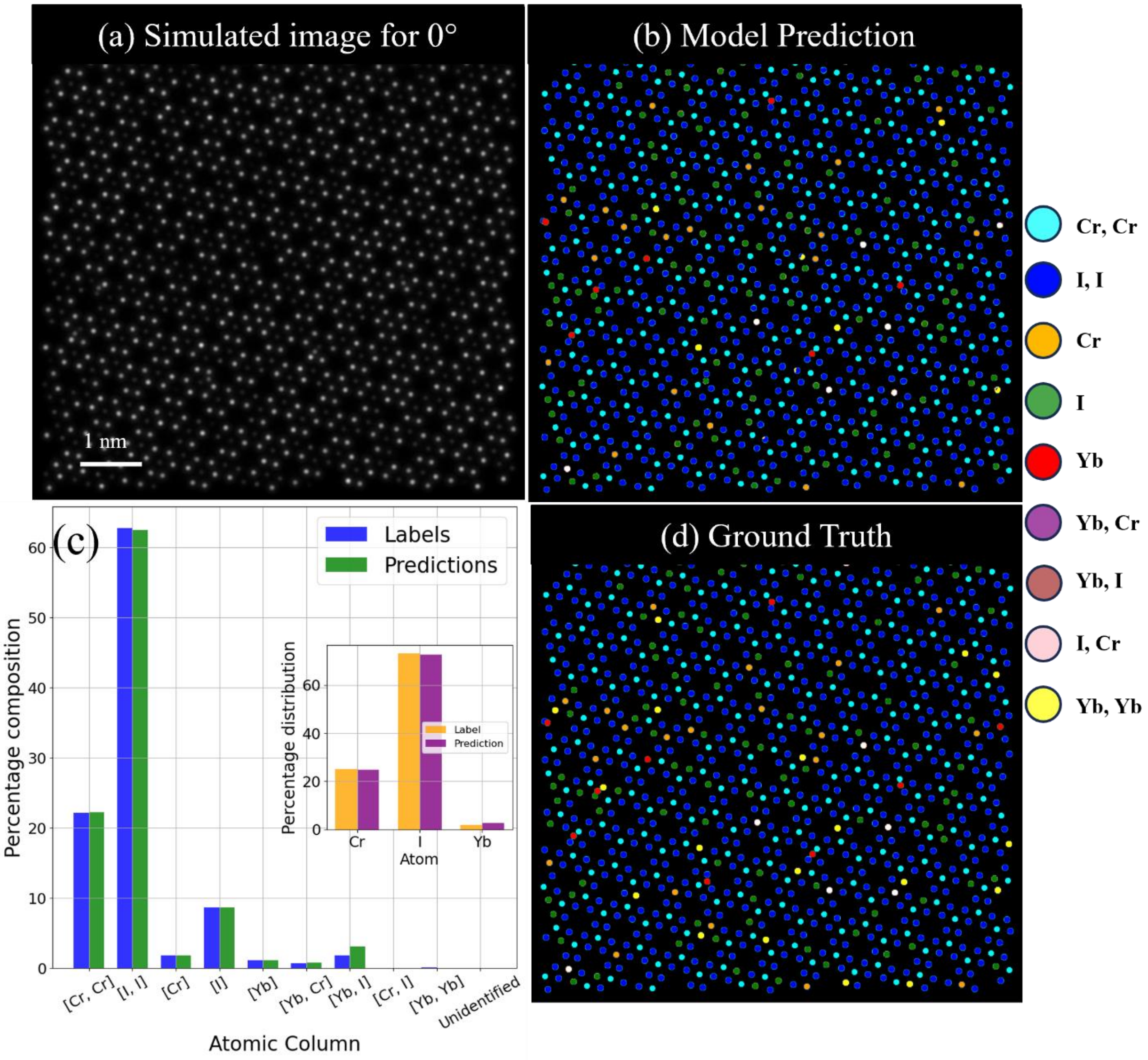

Figure 3.1. (a) Simulated STEM image for hBN-CrI$_3$ with 0° twist angle and (b) inference of the image by the trained U-Net. (c) quantitative comparison of atomic column predictions with ground truth (d) ground truth (actual atomic columns) for the image

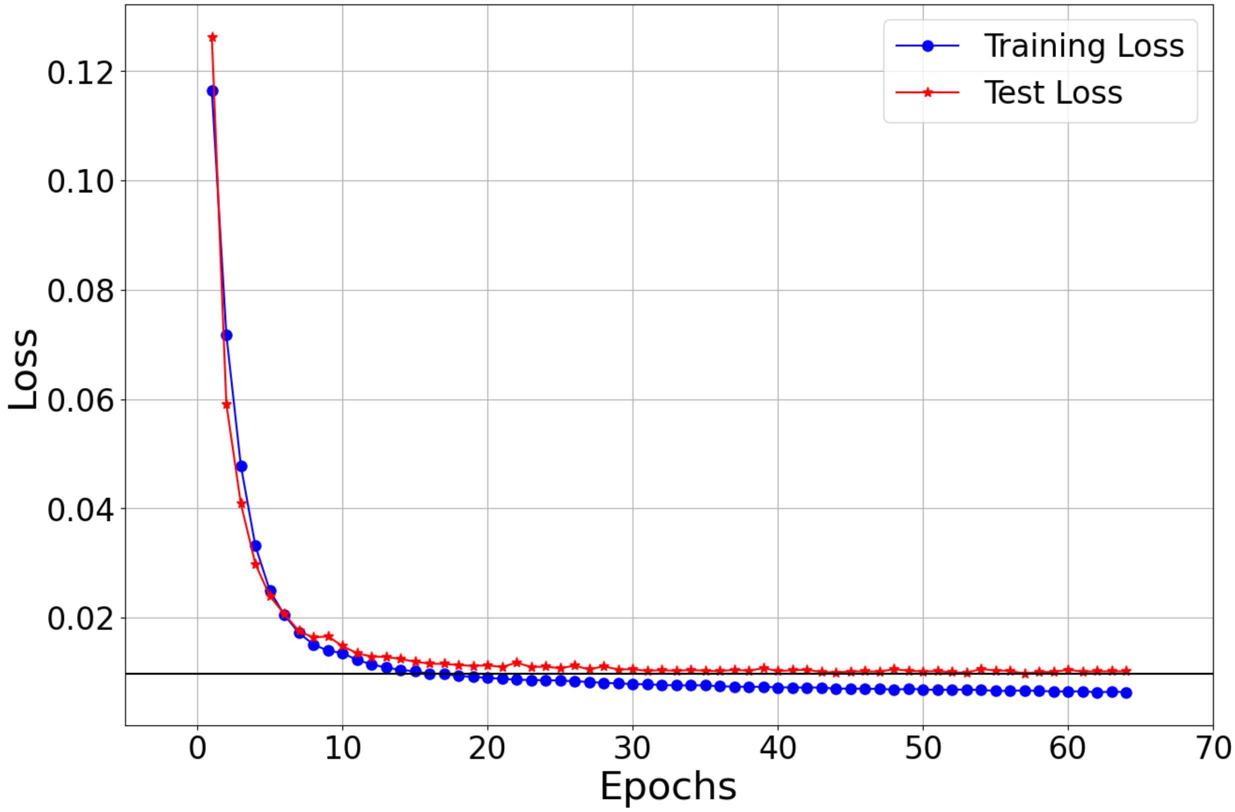

Figure 3.2. Curve for train loss and test loss v/s epoch for the first 65 epochs

Given that our model primarily focuses on bilayers and heterostructures, it is crucial to assess the model's performance across different atomic configurations. With this in mind, we trained the model on three twist angles for hBN-CrI_3 heterostructures; specifically, 0°, 1°, and 2°. The aim was to evaluate the model's performance when trained on different atomic configurations.

Upon assessment, we observe that the accuracy of classification obtained was 99.27% across all twist angles, which is consistent with a model trained and tested on a single twist angle. However, the artifacts of class imbalance were still evident. U-Net architecture consists of a softmax layer (an activation function that scales numbers into probabilities), which helps shaping the output of the model. Subsequently we take the class with the largest value indicating the most probable class, thus making the classification map consists only of integer data types. Bearing this in mind, we can employ binary masks to derive binary maps for each class. By utilizing these binary maps, we can determine the count of the respective atomic column by applying image processing techniques using OpenCV, giving us insights into the distribution of atomic columns in the STEM image, and consequently, the defect concentration.

Ultimately, we can ascertain the distribution of atomic columns and composition in our ADF-STEM image. It is also intriguing to observe the artifacts resulting from the moiré lattice for twisted bilayers, with notable features being the hexagonal trend in the [Cr, Cr], and [I, I] classes for 1°, 2°. Upon comparing the prediction results with the ground truth truth (actual atomic column classification labels from the simulations), we are confident that the model can be further refined to a point where it would be reliable enough for implementation in a STEM characterization workflow.

The proposed workflow enables us to generate a classification map in seconds, a task that would otherwise require significant man-hours if done manually, particularly for 2D bilayers or heterostructures. Additionally, due to the quick runtime, and the fact that the workflow is entirely developed using Python, a well-optimized U-Net can be easily incorporated right into NionSwift, an open-source scientific image processing software that integrates hardware control, data acquisition, visualization, processing, and analysis using Python [79]. This would allow real-time segmentation of atomic columns. Such a feature could be a valuable tool in dynamic studies performed using STEM.

The model was trained on images with an 8nm x 8nm field of view, and as a result, it will not perform well on STEM images with different magnifications. However, we believe that training the model on a range of magnifications could overcome this limitation. The limitations of the model appear to be largely due to the constraints of the training dataset. Therefore, optimizing the dataset generation workflow could potentially mitigate these discrepancies. The flexible architecture of our library facilitates the incorporation of such updates into the dataset generation branch. This adaptability is a key strength of our approach, allowing us to continually improve and refine our model's performance. Future work will focus on leveraging this flexibility to further enhance the model's capabilities.

In any case, the prediction results obtained gives us a proof of concept for our proposed python package. We conducted evaluation tests on images that were not part of the training data, such as those with different twist angles or those where Yb defects were replaced with other types of defects. Interestingly, the model demonstrated immaculate performance when tested on these unknown variables.

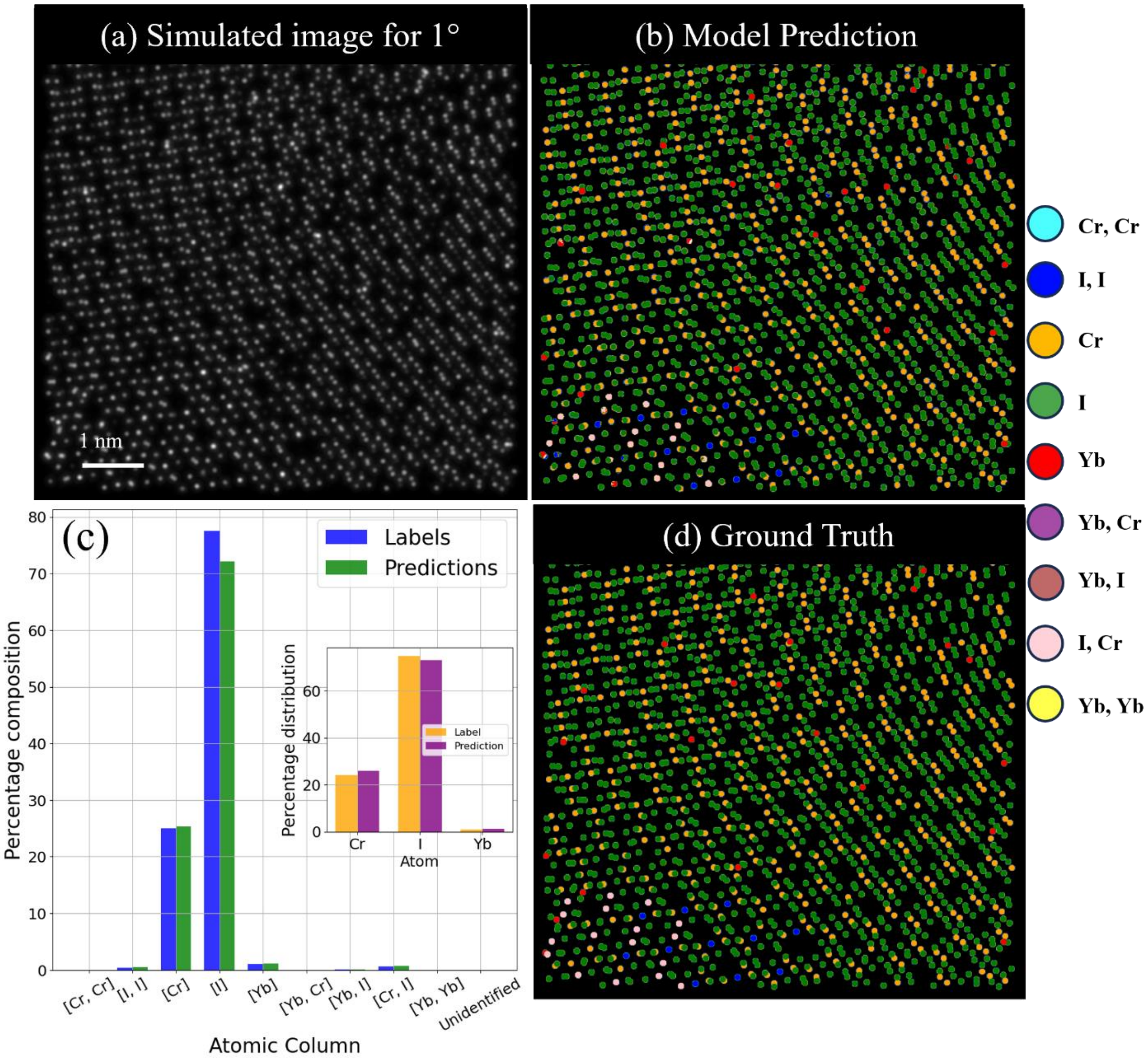

Figure 3.3. (a) Simulated STEM image for hBN-CrI_3 with 1° twist angle and (b) inference of the image by the trained U-Net. (c) quantitative comparison of atomic column predictions with ground truth (d) ground truth (actual atomic columns) for the image (scale bar = 1 nm)

3.2 PERFORMANCE OVER UNKNOWN TWIST ANGLE

Figure 3.4 illustrates the classification results obtained for a CrI_3 bilayer with a 3.5° twist angle. A comparison of the prediction (Fig. c) with the ground truth (Fig. b) reveals that the U-Net is capable of segmenting atomic columns with reasonable accuracy, even at unknown twist angles.

This is further substantiated by the model's performance for twist angles of 1.5°, 2.5°, and 4°, which is similar to that for 3.5°.

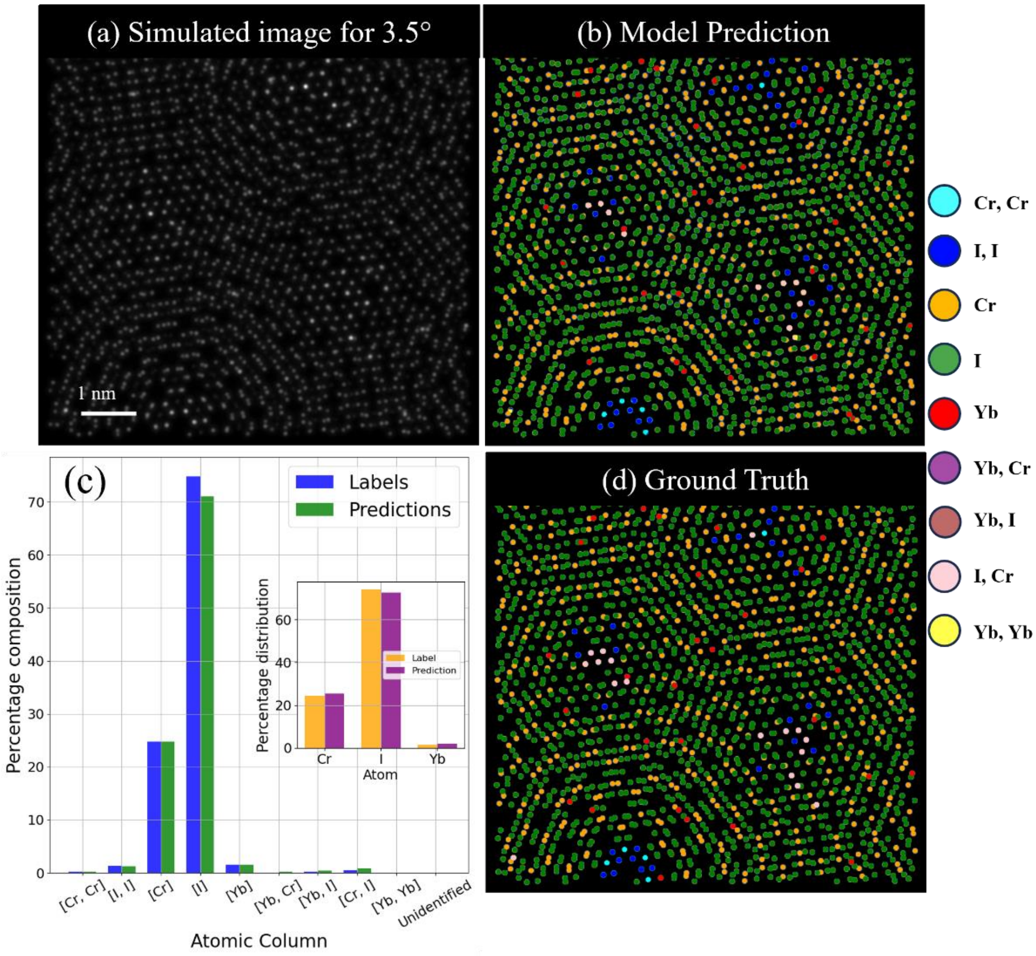

Figure 3.4. (a) Simulated STEM image for hBN-CrI_3 with unknown (3.5°) twist angle and (b) inference of the image by the trained U-Net. (c) quantitative comparison of atomic column predictions with ground truth (d) ground truth (actual atomic columns) for the image (scale bar = 1 nm)

3.3 PERFORMANCE OVER UNKNOWN DEFECT

In addition, along with an unknown twist angle of 4°, Yb defects were substituted with gadolinium (Gd) defects, which have atomic size and mass comparable to Yb. Figure 3.5 presents the classification results for one such case. The model's performance on unknown data, in conjunction with the trend in test/train loss versus epoch, provides strong evidence for the U-Net's potential to generalize the segmentation task over unknown data, albeit for a specific bulk that the model is trained on. This underscores the robustness and versatility of our proposed Python package.

As discussed previously, the analysis of STEM images often involves comparing the contrast of the atomic column with a simulated image. In instances where the contrast for two different atomic columns is similar, the full-width half-maxima (FWHM) is extracted to estimate the radius of the atom. For STEM images of relatively simple structures (such as graphene, WSe2, hBN monolayers with defects), exploring tree-based decision algorithms could be beneficial, especially if we heavily rely on such ground rules. Decision Trees or similar clustering algorithms require significantly smaller training data and are much more efficient in scenarios where access to GPU is limited. However, for specimens with sophisticated lattices, such as bilayers and heterostructures, decision trees may not be sufficiently reliable. Due to the number of features and the complexity of these features, a CNN would be the optimal choice for such classification tasks.

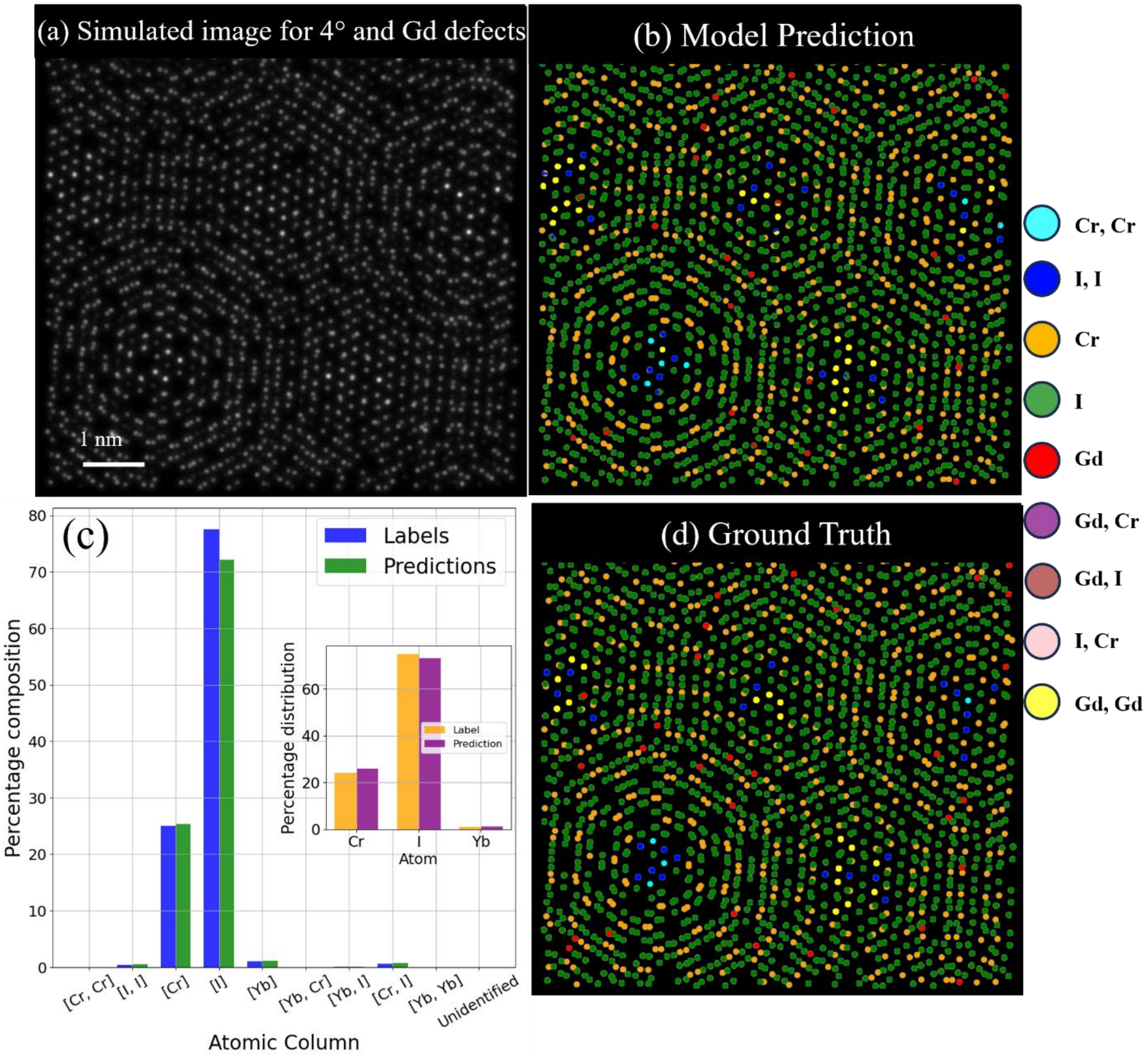

Figure 3.5. (a) Simulated STEM image for hBN-CrI_3 with 4° twist angle with Gd defects and (b) inference of the image by the trained U-Net. (c) quantitative comparison of atomic column predictions with ground truth (d) ground truth (actual atomic columns) for the image (scale bar = 1 nm)

3.4 FEATURE MAPS

The feature maps generated prior to the final softmax layer, as depicted in the figure 3.6, provide insightful observations. For twist angles of 0°, the U-Net effectively produces reliable feature maps, with negligible overlap or discrepancies in artifacts. This is inferred by comparing the activation results across each map to identify any significant overlap. Some misclassifications in atomic columns are observed when examining the binary class map for atomic column [Yb, I] in 0° twist, however, the relative size of these inaccuracies is overshadowed by the correct feature maps.

In contrast, for a twist angle of 1° (figure 3.7), artifacts in the column [Cr, Cr] exhibit inaccurate activation values that resemble thick rings. While this could potentially raise concerns, these artifacts are eliminated after the softmax layer. This issue could be linked to the different class distributions in 0° twist (where the majority of the columns are [Cr, Cr] and [I, I]), leading to such behavior for the non-zero twist angles (where the majority of columns are [Cr] and [I]).

It is worth noting that this can likely be mitigated by appropriately structuring the training data, such as ensuring a more diverse class count and a greater variety of atomic configurations. This observation underscores the importance of data structuring in enhancing the performance and accuracy of deep learning models in the analysis of 2D materials.

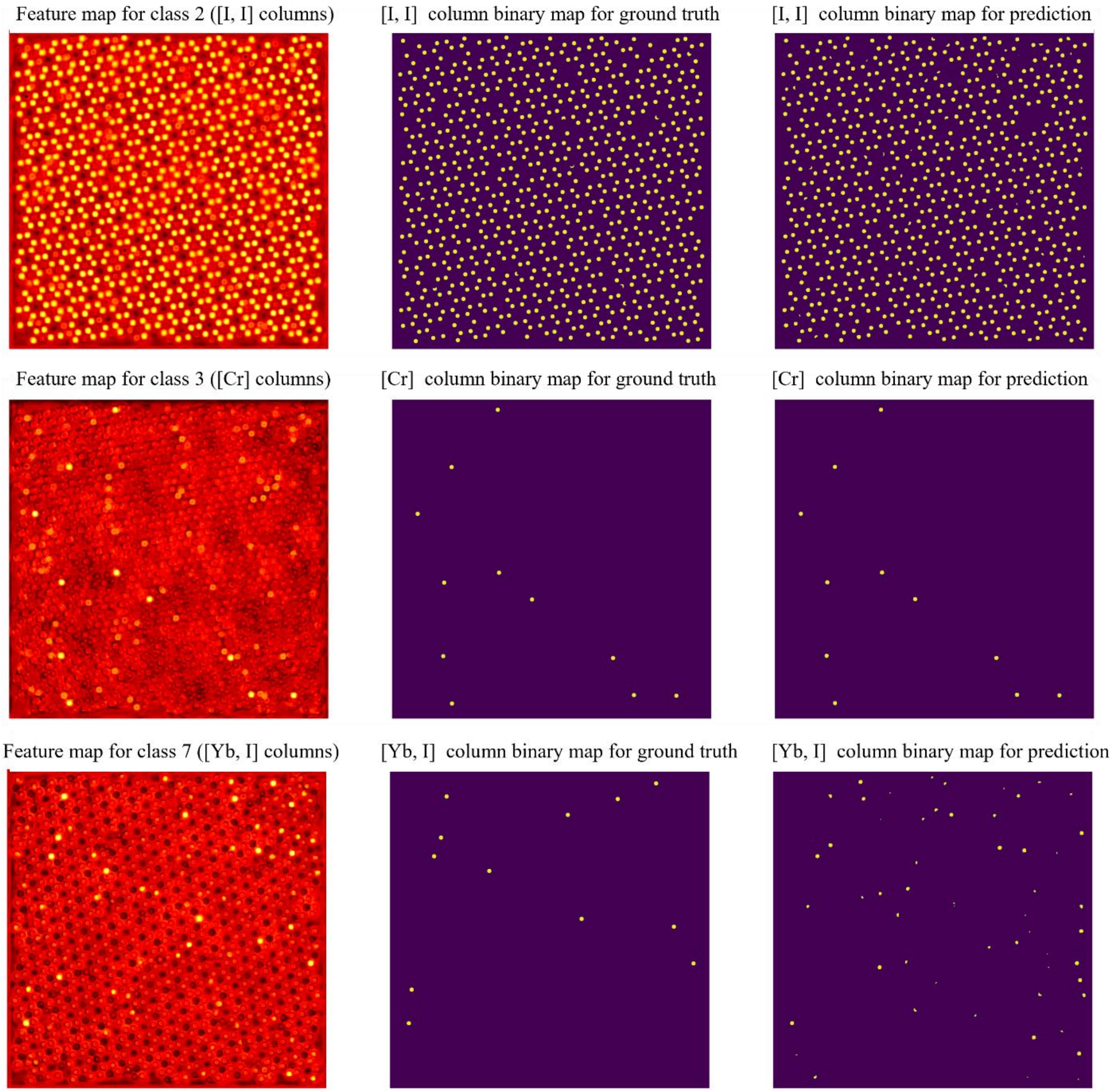

Figure 3.6. Figure shows a select few feature maps generated by the UNet for the final classification for input image with 0° twist angle. The feature maps included here are for the following classes of atomic columns: [Cr, Cr], [Yb], [Yb, I].

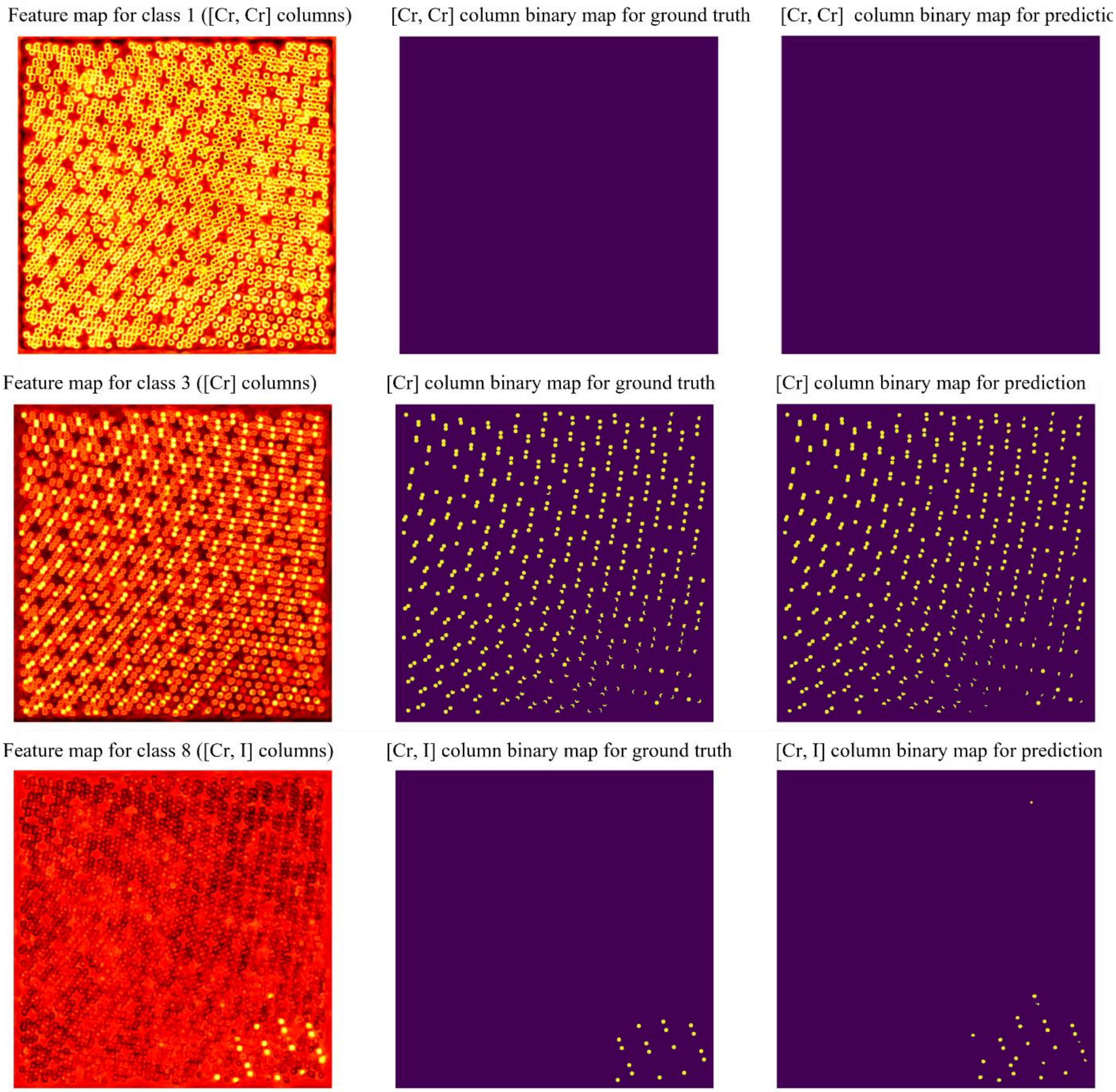

Figure 3.7. Figure shows a select few feature maps generated by the UNet for the final classification for input image with 1° twist angle. The feature maps included here are for the following classes of atomic columns: [Cr, Cr], [Yb], [Yb, I].

Chapter 4. CONCLUSION AND FUTURE WORK

4.1 CONCLUSION

In essence, we have established a Python repository dedicated to automating the creation of training datasets and training a U-Net architecture CNN for the classification of atomic columns. The repository is bifurcated into two sections: the simulator and the neural network, both of which can be conveniently utilized to set up and train a U-Net for any material of interest, albeit requiring access to a GPU for both tasks.

To showcase the potential of our library, we classified and quantified a range of atomic configurations for hBN encapsulated CrI_3 with remarkable precision. Upon evaluating the model's performance on unfamiliar training data, we are confident that our method can significantly reduce the workload and time required for interpreting STEM images of 2D material constructs.

The swift runtime for predictions underscores our model's capability to perform real-time dynamic studies. This also enables us to analyze the interaction of the specimen with the irradiating electron beam and conduct other such in-situ studies.

Considerable effort was invested in future-proofing the library to ensure its smooth expansion. One of the key factors was the flexibility of abTEM and the variety of features it includes. This flexibility could potentially allow us to broaden the code's inclusivity, not just for classification tasks, but also for general STEM image analysis techniques.

4.2 FUTURE WORK

A critical next step in future work involves benchmarking the classification results of our model with experimental images. Without a dependable denoising model, we would be limited to STEM images with a high SNR ratio and essentially, specimens with higher radiation tolerance.

Previous work on using simulated training dataset for training has demonstrated positive results with experimental STEM images for WSe_2, WS_2 [70], graphene, hBN, and gold nanoparticles [71]. Although these studies primarily focused on STEM images of monolayers, we are optimistic about our library's performance over experimental images for 2D layer heterostructures and bilayers.

The capabilities of our method should be tested with multiple defects, involving different atoms, to understand how well our model can generalize across a variety of atomic configurations and defects.

The performance of our model could be compared with other kinds of algorithms, such as decision trees. However, we believe that because of the amount of classes involved coupled with the complicated stoichiometries such as moiré, a sophisticated approach such as CNN would be the best option. An interesting work done on developing a combination of decision tree with a CNN has shown similar results as compared to CNN only methods.

The work presented in this thesis was made possible through the use of the University of Washington's supercomputer, Hyak. As a shared resource, managing storage space was a recurring challenge. A potential solution to this issue is the implementation of "training on the go," a process that involves simulating, training, and subsequently deleting a batch of images. The ability to define a seed for all random number generators ensures reproducibility of results, which facilitates improved maintenance and debugging for such training features.

Previously, it was mentioned that to set up and train a model, only the unit cells of the materials involved are required. This limitation can be overcome by using space groups to create the structures for simulations. While this approach may require additional setup efforts, the fact that all operations can be performed within the library itself presents a clear advantage. This approach would not only streamline the process but it would also enhance the flexibility and applicability of the method.

The quality of STEM images is a critical factor in the analysis of two-dimensional (2D) materials. The Signal-to-Noise Ratio (SNR) is particularly significant, as it directly impacts the interpretation of these images. Certain specimens, sensitive to electron radiation, necessitate a high scanning rate to minimize exposure to the electron beam. This can result in images with substantial noise, complicating the classification task and potentially leading to unreliable outcomes. Therefore, there is a need for a reliable method to enhance the SNR for improved analysis and interpretation of atomic columns.

CNNs also offer promising solutions to such challenges. Tools like abTEM, which allow for the inclusion of a variety of distortions/noise such as Poisson’s noise, scan noise, and aberrations, can be highly beneficial in training a robust denoising model. Utilizing the simulated dataset for our U-Net, the same input images can be employed to set up and train a denoising model. We performed some preliminary tests using an out-of-the-box denoising model which gave promising results, however requiring a significant amount of optimization.

Previous studies employing neural networks in STEM image classification have incorporated their own versions of denoising models. These models have demonstrated excellent results and shown great potential in experimental images [22].

However, in the case of moiré patterns for non-zero twist angles, it is observed that lighter atoms at the lowest column height are occasionally removed in the denoising process. Due to the lower contrast and size of the feature, such atoms are prone to be misidentified as noise and subsequently removed. This highlights the need for a denoising model, especially for moiré structures, to be meticulously optimized.

BIBLIOGRAPHY

[1] Wang, H.; Zhao, Y.; Xie, Y.; Ma, X.; Zhang, X. *Recent progress in synthesis of two-dimensional hexagonal boron nitride*. J. Semicond. 2017, 38 (3), 031003

[2] Shi, Y.; Hamsen, C.; Jia, X.; Kim, K. K.; Reina, A.; Hofmann, M.; Hsu, A. L.; Zhang, K.; Li, H.; Juang, Z.-Y. et al. *Synthesis of few-layer hexagonal boron nitride thin film by chemical vapor deposition*. Nano Lett. 2010, 10 (10), 4134– 4139 3.

[3] Meng, J.; Wang, D.; Cheng, L.; Gao, M.; Zhang, X. *Recent progress in synthesis, properties, and applications of hexagonal boron nitride-based heterostructures*. Nanotechnology 2019, 30 (7), 074003

[4] Han, S.A., Bhatia, R. & Kim, SW. *Synthesis, properties and potential applications of two-dimensional transition metal dichalcogenides*. Nano Convergence 2, 17 (2015).

[5] Yin, X.; Tang, C. S.; Zheng, Y.; Gao, J.; Wu, J.; Zhang, H.; Chhowalla, M.; Chen, W.; Wee, A. T. S. *Recent developments in 2D transition metal dichalcogenides: phase transition and applications of the (quasi-)metallic phases*. Chem. Soc. Rev. 2021, 50, 10087-10115

[6] Xiao, Y.; Xiong, C.; Chen, M.-M.; Wang, S.; Fu, L.; Zhang, X. *Structure modulation of two-dimensional transition metal chalcogenides: recent advances in methodology, mechanism and applications.* Chem. Soc. Rev. 2023, 52, 1215-1272.

[7] Huang, B., Clark, G., Navarro-Moratalla, E. et al. *Layer-dependent ferromagnetism in a van der Waals crystal down to the monolayer limit*. Nature 546, 270–273 (2017)

[8] Qiu, Z., Holwill, M., Olsen, T. et al. *Visualizing atomic structure and magnetism of 2D magnetic insulators via tunneling through graphene*. Nat Commun 12, 70 (2021).

[9] Liang, Q.; Zhang, Q.; Zhao, X.; Liu, M.; Wee, A. T. S. *Defect Engineering of Two-Dimensional Transition-Metal Dichalcogenides: Applications, Challenges, and Opportunities.* ACS Nano 2021, 15 (2), 2165-2181.

[10] Lin, Z.; Carvalho, B. R.; Kahn, E.; Lv, R.; Rao, R.; Terrones, H.; Pimenta, M. A.; Terrones, M. *Defect engineering of two-dimensional transition metal dichalcogenides*. 2D Mater. 2016, 3 (2), 022002.

[11] Xiong, Z.; Zhong, L.; Wang, H.; Li, X. *Structural Defects, Mechanical Behaviors, and Properties of Two-Dimensional Materials*. Materials (Basel). 2021, 14 (5), 1192

[12] Tripathi, M.; Lee, F.; Michail, A.; Anestopoulos, D.; McHugh, J. G.; Ogilvie, S. P.; Large, M. J.; Graf, A. A.; Lynch, P. J.; Parthenios, J.; Papagelis, K.; Roy, S.; Saadi, M. A. S. R.; Rahman, M. M.; Pugno, N. M.; King, A. A. K.; Ajayan, P. M.; Dalton, A. B. *Structural Defects Modulate Electronic and Nanomechanical Properties of 2D Materials*. ACS Nano 2021, 15 (2), 2520-2531.

[13] Jiang, D.; Liu, Z.; Xiao, Z.; Qian, Z.; Sun, Y.; Zeng, Z.; Wang, R. *Flexible electronics based on 2D transition metal dichalcogenides*. J. Mater. Chem. A 2022, 10, 89-121

[14] Kim, S. J.; Choi, K.; Lee, B.; Kim, Y.; Hong, B. H. *Materials for flexible, stretchable electronics: graphene and 2D materials*. Annu. Rev. Mater. Res. 2015, 45, 63– 84

[15] Bolotsky, A.; Butler, D.; Dong, C.; Gerace, K.; Glavin, N.; Muratore, C.; Robinson, J. A.; Ebrahimi, A. *Two-Dimensional Materials in Biosensing and Healthcare: From in Vitro Diagnostics to Optogenetics and beyond*. ACS Nano 2019, 13 (9), 9781-9810.

[16] Rohaizad, N.; Mayorga-Martinez, C. C.; Fojtů, M.; Latiff, N. M.; Pumera, M. *Two-dimensional materials in biomedical, biosensing and sensing applications*. Chem. Soc. Rev. 2021, 50, 619-657

[17] Dervin, S.; Dionysiou, D. D.; Pillai, S. C. *2D nanostructures for water purification: graphene and beyond.* Nanoscale 2016, 33, 022002.

[18] Raza, S.; Ghasali, E.; Orooji, Y.; Lin, H.; Karaman, C.; Dragoi, E. N.; Erk, N. *Two dimensional (2D) materials and biomaterials for water desalination; structure, properties, and recent advances*. Environmental Research 2023, 219, 114998

[19] Xia, F.; Wang, H.; Xiao, D.; Dubey, M.; Ramasubramaniam, *A. Two-dimensional material nanophotonics*. Nature Photonics 2014, 8 (12), 899-907.

[20] Xia, F., Wang, H., Xiao, D. et al. *Two-dimensional material nanophotonics*. Nature Photon 8, 899–907 (2014)

[21] Koppens, F. H. L. et al. *Photodetectors based on graphene, other two-dimensional materials and hybrid systems.* Nat. Nanotechnol. 9, 780–793 (2014).

[22] Kennes, D. M. et al. *Moiré heterostructures as a condensed-matter quantum simulator*. Nat. Phys. 17, 155–163 (2021)

[23] Mak, K. F., Lee, C., Hone, J., Shan, J. & Heinz, T. F. *Atomically thin MoS2: a new direct-gap semiconductor*. Phys. Rev. Lett. 105, 136805 (2010).

[24] Radisavljevic, B., Radenovic, A., Brivio, J., Giacometti, V. & Kis, A. *Single-layer MoS2 transistors*. Nat. Nanotechnol. 6, 147–150 (2011).

[25] Yang, H., Valenzuela, S.O., Chshiev, M. et al. *Two-dimensional materials prospects for non-volatile spintronic memories*. Nature 606, 663–673 (2022).

[26] Wang, H.; Wen, Y.; Zeng, H.; Xiong, Z.; Tu, Y.; Zhu, H.; Cheng, R.; Yin, L.; Jiang, J.; Zhai, B.; Liu, C.; Shan, C.; He, J. *Two-Dimensional Ferroic Materials for Non-volatile Memory Applications*. Advanced Materials 2023, e2305044.

[27] Pal, A.; Zhang, S.; Chavan, T.; Agashiwala, K.; Yeh, C.-H.; Cao, W.; Banerjee, K. *Quantum-Engineered Devices Based on 2D Materials for Next-Generation Information Processing and Storage*. Advanced Materials 2022

[28] A. W. A. Murphy, Z. Liu, A. V. Gorbach, A. Ilie, V. K. Valev*, Doubly-Resonant Enhancement of Second Harmonic Generation from a WS2 Nanomesh Polymorph with a Modified Energy Landscape*. Laser & Photonics Reviews 2021, 15, 2100117.

[29] Stern, H.L., Gu, Q., Jarman, J. et al. *Room-temperature optically detected magnetic resonance of single defects in hexagonal boron nitride*. Nat Commun 13, 618 (2022).

[30] He, F.; Zhou, Y.; Ye, Z.; Cho, S.-H.; Jeong, J.; Meng, X.; Wang, Y. *Moiré Patterns in 2D Materials: A Review*. ACS Nano 2021, 15 (4), 5944-5958.

[31] Tong, Q.; Liu, F.; Xiao, J.; Yao, W. *Skyrmions in the Moiré of van der Waals 2D Magnets*. Nano Letters 2018.

[32] Xu, Q.; Guo, Y.; Xian, L. *Moiré flat bands in twisted 2D hexagonal vdW materials*. 2D Mater. 2022, 9 (1), 014005

[33] Tong, Q., Yu, H., Zhu, Q. et al. *Topological mosaics in moiré superlattices of van der Waals heterobilayers.* Nature Phys 13, 356–362 (2017)

[34] Kezilebieke, S.; Vaňo, V.; Huda, M. N.; Aapro, M.; Ganguli, S. C.; Liljeroth, P.; Lado, J. L. *Moiré-Enabled Topological Superconductivity*. Nano Lett. 2022, 22 (1), 328–333

[35] Sivadas, N.; Okamoto, S.; Xu, X.; Fennie, C. J.; Xiao, D. *Stacking-Dependent Magnetism in Bilayer CrI3*. Nano Lett. 2018, 18 (12), 7658–7664.

[36] Kong, X.; Yoon, H.; Han, M. J.; Liang, L. *Switching interlayer magnetic order in bilayer CrI3 by stacking reversal*. Nanoscale 2021, 13, 16172-16181.

[37] Beck, R. A.; Lu, L.; Sushko, P. V.; Xu, X.; Li, X. *Defect-Induced Magnetic Skyrmion in a Two-Dimensional Chromium Triiodide Monolayer*. JACS Au 2021, 1 (9), 1362–1367.

[38] Cheng, X., Cheng, Z., Wang, C. et al. *Light helicity detector based on 2D magnetic semiconductor CrI3*. Nat Commun 12, 6874 (2021).

[39] Song T, Sun QC, Anderson E, Wang C, Qian J, Taniguchi T, Watanabe K, McGuire MA, Stöhr R, Xiao D, Cao T, Wrachtrup J, Xu X. *Direct visualization of magnetic domains and moiré magnetism in twisted 2D magnets*. Science. 2021 Nov 26;374(6571):1140-1144.

[40] León, A.M., Velásquez, É.A., Caro-Lopera, F. and Mejía-López, J. (2022), *Tuning Magnetic Order in CrI3 Bilayers via Moiré Patterns*. Adv. Theory Simul., 5: 2100307

[41] Pressler, K.; Snoeren, T. J.; Walsh, K. M.; Gamelin, D. R. *Magnetic Amplification at Yb3+ "Designer Defects" in the van der Waals Ferromagnet CrI3*. Nano Lett. 2023, 23 (4), 1320–1326.

[42] Zhang, J.; Guo, Y.; Li, P.; Wang, J.; Zhou, S.; Zhao, J.; Guo, D.; Zhong, D. *Imaging Vacancy Defects in Single-Layer Chromium Triiodide*. J. Phys. Chem. Lett. 2021, 12 (9), 2199–2205.

[43] Xu, Y., Ray, A., Shao, YT. et al. *Coexisting ferromagnetic–antiferromagnetic state in twisted bilayer CrI3*. Nat. Nanotechnol. 17, 143–147 (2022)

[44] Hennighausen, Z.; Kar, S. *Twistronics: a turning point in 2D quantum materials*. Electronic Structure 2021, 3 (1), 014004

[45] Jingyue (Jimmy) Liu, *Advances and Applications of Atomic-Resolution Scanning Transmission Electron Microscopy*, Microscopy and Microanalysis, Volume 27, Issue 5, 1 October 2021, Pages 943–995

[46] Ryo Ishikawa, Yu Jimbo, Mitsuhisa Terao, Masashi Nishikawa, Yujiro Ueno, Shigeyuki Morishita, Masaki Mukai, Naoya Shibata, Yuichi Ikuhara, *High spatiotemporal-resolution imaging in the scanning transmission electron microscope*, Microscopy, Volume 69, Issue 4, August 2020, Pages 240–247

[47] Jingyue (Jimmy) Liu, *Advances and Applications of Atomic-Resolution Scanning Transmission Electron Microscopy*, Microscopy and Microanalysis, Volume 27, Issue 5, 1 October 2021, Pages 943–995

[48] Egerton R F 2011 *Electron energy-loss spectroscopy in the electron microscope*, 3rd edition. (New York-Dordrecht-Heidelberg-London: Springer)

[49] Crozier PA, Chenna S. *In situ analysis of gas composition by electron energy-loss spectroscopy for environmental transmission electron microscopy*. Ultramicroscopy. 2011 Feb;111(3):177-85

[50] Ye-Jin Kim, Levi D. Palmer, Wonseok Lee, Nicholas J. Heller, Scott K. Cushing; *Using electron energy-loss spectroscopy to measure nanoscale electronic and vibrational dynamics in a TEM*. J. Chem. Phys. 7 August 2023; 159 (5): 050901

[51] Aronova MA, Leapman RD. *Development of Electron Energy Loss Spectroscopy in the Biological Sciences*. MRS Bull. 2012 Jan;37(1):53-62

[52] Krivanek, O., Chisholm, M., Nicolosi, V. et al. *Atom-by-atom structural and chemical analysis by annular dark-field electron microscopy*. Nature 464, 571–574 (2010).

[53] J. M. Cowley and A. F. Moodie (1957). "*The Scattering of Electrons by Atoms and Crystals. I. A New Theoretical Approach*". Acta Crystallographica. Vol. 10

[54] Kirkland, Earl J.. “*Image Simulation in Transmission Electron Microscopy*.” (2006).

[55] C. T. Koch,Ph.D. Thesis, Arizona Stete University, Tempe, Arizona,2002.

[56] Jacob Madsen and Toma Susi. *The abTEM code: transmission electron microscopy from first principles*. Open Research Europe 1:24, 2021

[57] Rocklin, M. (2015). *Dask: Parallel computation with blocked algorithms and task scheduling*. In Proceedings of the 14th python in science conference.

[58] Roy, W. Choi, S. Jeon, D. H. Kim, H. Kim, S. J. Yun, Y. Lee, J. Lee,Y.-M. Kim, J. Kim,Nano Lett.2018,18, 4523

[59] Azizi, Y. X. Wang, G. Stone, A. L. Elias, Z. Lin, M. Terrones, V. H.Crespi, N. Alem,Nano Lett.2017,17, 2802; b) D. Rhodes, D. A. Ch-enet, B. E. Janicek, C. Nyby, Y. Lin, W. Jin, D. Edelberg, E. Mannebach,N. Finney, A. Antony, T. Schiros, T. Klarr, A. Mazzoni, M. Chin, Y. C.Chiu,W.Zheng,Q.R.Zhang,F.Ernst,J.I.Dadayp,X.Tong,J.Ma,R.Lou, S. Wan, T. Qian, H. Ding, R. M. Osgood, D. W. Paley, A. M. Lin-denberg, P. Y. Huang, A. N. Pasupathy, M. Dubey, J. Hone, L. Balicas,Nano Lett.2017,17, 1616

[60] D. Sharma, I. Mishra, R. Parepalli and J. S, "*Biomedical Image Classification Using Convolutional Neural Networks*," 2023 International Conference on Intelligent and Innovative Technologies in Computing, Electrical and Electronics (IITCEE), Bengaluru, India, 2023, pp. 840-845

[61] Lee, K.-H.; Lee, H. W.; Yun, G. *A defect detection framework using three-dimensional convolutional neural network (3D-CNN) with in-situ monitoring data in laser powder bed fusion process*. Optics and Laser Technology 2023, 165, 109571.

[62] Sharma, N.; Jain, V.; Mishra, A. *An Analysis Of Convolutional Neural Networks For Image Classification*. Procedia Computer Science 2018, 132, 377-384.

[63] N. Jmour, S. Zayen and A. Abdelkrim, "*Convolutional neural networks for image classification*," 2018 International Conference on Advanced Systems and Electric Technologies (IC_ASET), Hammamet, Tunisia, 2018, pp. 397-402

[64] Ronneberger, O., Fischer, P., Brox, T. (2015*). U-Net: Convolutional Networks for Biomedical Image Segmentation*. In: Navab, N., Hornegger, J., Wells, W., Frangi, A. (eds) Medical Image Computing and Computer-Assisted Intervention – MICCAI 2015. MICCAI 2015. Lecture Notes in Computer Science(), vol 9351. Springer, Cham.

[65] J. McGlinchy, B. Johnson, B. Muller, M. Joseph and J. Diaz, "*Application of UNet Fully Convolutional Neural Network to Impervious Surface Segmentation in Urban Environment from High Resolution Satellite Imagery*," IGARSS 2019 - 2019 IEEE International Geoscience and Remote Sensing Symposium, Yokohama, Japan, 2019, pp. 3915-3918

[66] N. Siddique, S. Paheding, C. P. Elkin and V. Devabhaktuni, "*U-Net and Its Variants for Medical Image Segmentation: A Review of Theory and Applications*," in IEEE Access, vol. 9, pp. 82031-82057, 2021

[67] Cao, Y., Liu, S., Peng, Y. and Li, J. (2020), *DenseUNet: densely connected UNet for electron microscopy image segmentation*. IET Image Process., 14: 2682-2689

[68] Tsalera E, Papadakis A, Samarakou M, Voyiatzis I. *Feature Extraction with Handcrafted Methods and Convolutional Neural Networks for Facial Emotion Recognition*. Applied Sciences. 2022; 12(17):8455

[69] Teodoro, A.A.M., Silva, D.H., Saadi, M. et al. *An Analysis of Image Features Extracted by CNNs to Design Classification Models for COVID-19 and Non-COVID-19*. J Sign Process Syst 95, 101–113 (2023)

[70] Yang SH, Choi W, Cho BW, Agyapong-Fordjour FO, Park S, Yun SJ, Kim HJ, Han YK, Lee YH, Kim KK, Kim YM. *Deep Learning-Assisted Quantification of Atomic Dopants and Defects in 2D Materials*. Adv Sci (Weinh). 2021 Aug;8(16):e2101099

[71] Lin, R., Zhang, R., Wang, C. et al. *TEMImageNet training library and AtomSegNet deep-learning models for high-precision atom segmentation, localization, denoising, and deblurring of atomic-resolution images*. Sci Rep 11, 5386 (2021).

[72] Madsen, J., Liu, P., Kling, J., Wagner, J.B., Hansen, T.W., Winther, O. and Schiøtz, J. (2018), *A Deep Learning Approach to Identify Local Structures in Atomic-Resolution Transmission Electron Microscopy Images*. Adv. Theory Simul., 1: 1800037

[73] Hovden, R., Xin, H. L. & Muller, D. *A. Channeling of a subangstrom electron beam in a crystal mapped to two-dimensional molecular orbitals*. Phys. Rev. B 86, 195415

[74] Ask Hjorth Larsen, Jens Jørgen Mortensen, Jakob Blomqvist, Ivano E Castelli, Rune Christensen, Marcin Dułak, Jesper Friis, Michael N Groves, Bjørk Hammer, Cory Hargus, Eric D Hermes, Paul C Jennings, Peter Bjerre Jensen, James Kermode, John R Kitchin, Esben Leonhard Kolsbjerg, Joseph Kubal, Kristen Kaasbjerg, Steen Lysgaard, Jón Bergmann Maronsson, Tristan Maxson, Thomas Olsen, Lars Pastewka, Andrew Peterson, Carsten Rostgaard, Jakob Schiøtz, Ole Schütt, Mikkel Strange, Kristian S Thygesen, Tejs Vegge, Lasse Vilhelmsen, Michael Walter, Zhenhua Zeng, and Karsten W Jacobsen. *The atomic simulation environment — a python library for working with atoms*. Journal of Physics: Condensed Matter, 29(27):273002, 2017.

[75] Harris, C.R., Millman, K.J., van der Walt, S.J. et al. *Array programming with NumPy*. Nature 585, 357–362 (2020).

[76] Grenander, Ulf (1959). *Probability and Statistics: The Harald Cramér Volume*. Wiley. The Nyquist frequency is that frequency whose period is two sampling intervals

[77] Jafari, M. et al. (2019). *FU-Net: Multi-class Image Segmentation Using Feedback Weighted U-Net*. In: Zhao, Y., Barnes, N., Chen, B., Westermann, R., Kong, X., Lin, C. (eds) Image and Graphics. ICIG 2019. Lecture Notes in Computer Science(), vol 11902. Springer, Cham.

[78] S.J.Yun,D.L.Duong,D.M.Ha,K.Singh,T.L.Phan,W.Choi,Y.-M. Kim, Y. H. Lee,Adv. Sci.2020,7, 1903076 ACS Appl. Nano Mater.2021,4, 769

[79] Chris Meyer, Niklas Dellby, Jordan A Hachtel, Tracy Lovejoy, Andreas Mittelberger, Ondrej Krivanek, Nion Swift: Open Source Image Processing Software for Instrument Control, Data Acquisition, Organization, Visualization, and Analysis Using Python., Microscopy and Microanalysis, Volume 25, Issue S2, 1 August 2019, Pages 122–123

[80] This work was facilitated through the use of advanced computational, storage, and networking infrastructure provided by the Hyak supercomputer system and funded by the STF at the University of Washington.

[81] Quote by the Khajit from The Elder Scrolls V: Skyrim. Bethesda Game Studios. (2011)